AFRL-VS-HA-TR-2005-1050

Improved Surface Wave Dispersion Models, Amplitude Measurements and Azimuth Estimates

J.L. Stevens
D.A. Adams
G.E. Baker
M.G. Eneva
H. Xu

Science Applications International Corporation
10260 Campus Point Drive
San Diego, CA 92121-1578

13 March 2005

Final Report

AIR FORCE RESEARCH LABORATORY
Space Vehicles Directorate
29 Randolph Rd
AIR FORCE MATERIEL COMMAND
Hanscom AFB, MA 01731-3010

This technical report has been reviewed and is approved for publication.

AFRL-VS-HA-TR-2005-1050

/signed/

ROBERT A. RAISTRICK
Contract Manager

/signed/

ROBERT BELAND, Chief
Battlespace Surveillance Innovation Center

This report has been reviewed by the ESC Public Affairs Office (PA) and is releasable to the National Technical Information Service (NTIS).

Qualified requestors may obtain additional copies form the Defense Technical Information Center (DTIC). All others should apply to the National Technical Information Service.

If your address has changed, if you with to be removed from the mailing list, or if the addressee is no longer employed by your organization, please notify AFRL/VSIM, 29 Randolph Rd., Hanscom AFB, MA 01731-3010. This will assist us in maintaining a current mailing list.

Do not return copies of this report unless contractual obligations or notices on a specific document require that it be returned.

Using Government drawings, specifications, or other data included in this document for any purpose other than Government procurement does not in any way obligate the U.S. Government. The fact that the Government formulated or supplied the drawings, specifications, or other data does not license the holder or any other person or corporation; or convey any rights or permission to manufacture, use, or sell any patented invention that may relate to them.

This report is published in the interest of scientific and technical information exchange and its publication does not constitute the Government's approval or disapproval of its ideas or findings.

REPORT DOCUMENTATION PAGE

Form Approved
OMB No. 0704-0188

1. REPORT DATE *(DD-MM-YYYY)*	2. REPORT TYPE	3. DATES COVERED *(From - To)*
31-03-2005	Final	25 Sept 2001 – 31 March 2005

4. TITLE AND SUBTITLE
Improved Surface Wave Dispersion Models, Amplitude Measurements and Azimuth Estimates

5a. CONTRACT NUMBER
DTRA01-01-C-0082

5b. GRANT NUMBER

5c. PROGRAM ELEMENT NUMBER

6. AUTHOR(S)
Jeffry L. Stevens, David A. Adams, G. Eli Baker, Mariana G. Eneva, and Heming Xu

5d. PROJECT NUMBER
DTRA

5e. TASK NUMBER
OT

5f. WORK UNIT NUMBER
A1

7. PERFORMING ORGANIZATION NAME(S) AND ADDRESS(ES)

Science Applications International Corporation
10260 Campus Point Drive
San Diego, CA 92121

8. PERFORMING ORGANIZATION REPORT NUMBER

9. SPONSORING / MONITORING AGENCY NAME(S) AND ADDRESS(ES)
Air Force Research Laboratory
29 Randolph Road
Hanscom AFB, MA 01731-3010

10. SPONSOR/MONITOR'S ACRONYM(S)
AFRL/VSBYE

11. SPONSOR/MONITOR'S REPORT NUMBER(S)
AFRL-VS-HA-TR-2005-1050

12. DISTRIBUTION / AVAILABILITY STATEMENT
Approved for Public Release; Distribution Unlimited.

13. SUPPLEMENTARY NOTES

14. ABSTRACT

The goal of this project is to reduce the magnitude threshold for which surface waves can be identified and measured reliably, and to improve the accuracy of surface wave measurement, using phase-matched filtering and global regionalized earth and dispersion models. Significant products and results of this work include: 1) assembly of a data set of dispersion measurements of over one million data points; 2) tomographic inversion of this data set for global earth and dispersion models; 3) implementation and testing of an improved azimuth estimation technique using Rayleigh wave polarization; 4) implementation and testing of a path corrected spectral magnitude. The path corrected spectral magnitude is a "regional Ms" which has been a long-term goal of this program. The global earth and dispersion models are available on request to other researchers working in this program.

15. SUBJECT TERMS
Rayleigh wave, Dispersion, Magnitude, Polarization, Global tomography

16. SECURITY CLASSIFICATION OF:			17. LIMITATION OF ABSTRACT	18. NUMBER OF PAGES	19a. NAME OF RESPONSIBLE PERSON
a. REPORT	b. ABSTRACT	c. THIS PAGE			Robert J. Raistrick
UNCLAS	UNCLAS	UNCLAS	SAR	72	19b. TELEPHONE NUMBER *(include area code)* 781-377-3726

ABSTRACT

The goal of this project is to reduce the magnitude threshold for which surface waves can be identified and measured reliably, and to improve the accuracy of surface wave measurement, using phase-matched filtering and global regionalized earth and dispersion models. Significant products and results of this work include: 1) assembly of a data set of dispersion measurements of over one million data points; 2) tomographic inversion of this data set for global earth and dispersion models; 3) implementation and testing of an improved azimuth estimation technique using Rayleigh wave polarization; 4) implementation and testing of a path corrected spectral magnitude. The path corrected spectral magnitude is a "regional M_s" which has been a long-term goal of this program. The global earth and dispersion models are available on request to other researchers working in this program.

TABLE OF CONTENTS

LIST OF FIGURES

LIST OF TABLES

Page

PREFACE

We would like to thank Mike Ritzwoller, Anatoli Levshin and Nikolai Shapiro of the University of Colorado, Bob Herrmann of St. Louis University, and other researchers who have allowed us to use their data in this project. Much of the work described in this report has been presented in three Seismic Research Review papers (Stevens et al, 2002, 2003 and 2004). The material in section 6 has been published in Geophysical Research Letters (Baker and Stevens, 2004).

1 EXECUTIVE SUMMARY

The primary goal of this project is to reduce the magnitude threshold for which surface waves can be identified and measured reliably, and to improve the accuracy of surface wave measurement, using phase-matched filtering and global regionalized earth and dispersion models. Following are the most significant products and results of this work:

1. We assembled a dataset of dispersion measurements of over one million data points. Some of this dataset came from our own measurements, but most came from other research studies, and we thank all of those scientists who have contributed to this effort. This dataset is one of the largest dispersion datasets ever assembled and is particularly unique in its coverage for a broad range of frequencies.

2. We developed and have continuously improved a set of global earth models and dispersion models defined on a one-degree grid. These models were developed by simultaneously inverting the entire dataset for a set of earth structures, which in turn allow surface wave dispersion to be calculated between any two points on the earth at any set of frequencies, with the dispersion models constrained by the large dataset. These global earth and dispersion models are available on request to other researchers working in this program.

3. We implemented the azimuth estimation technique developed by Selby using Chael's algorithm, tested it on a large dataset of International Monitoring System (IMS) data, and demonstrated that it is a major improvement over other commonly used azimuth estimation techniques. This azimuth estimation technique can be used together with the existing detection test, which is based on consistency of measurement with surface wave dispersion maps, to reduce the detection threshold for which surface waves can be reliably identified and measured.

4. We implemented and tested a path corrected spectral magnitude, developed procedures for optimizing it and evaluated the discrimination capability of this and other types of surface wave measurements. Two important results of this work are:

    a. The path corrected spectral magnitude is independent of distance and unaffected by dispersion and therefore can be measured at any distance, including very close to the source, and it will have the same value as a measurement made at a greater distance. The path corrected spectral magnitude is therefore a "regional M_s" which has been a long-term goal of this program.

    b. For discrimination purposes, surface waves should be measured at periods greater than 10 seconds. Periods of 10 seconds and longer can be measured even at very close range, and there is little or no S/N improvement at shorter periods. Discrimination is degraded at higher frequencies due to the decrease in earthquake spectral amplitude relative to explosions at higher frequencies.

5. We performed a study of "problem cases", where surface wave dispersion and/or amplitudes are inconsistent with model predictions. Typically these cases occur where there are strong heterogeneities in earth structure along the path, particularly for grazing incidence along large changes in material properties. Ray theory predicts that surface waves will take the minimum time path between the source and receiver in such cases, but the observed waveforms are considerably more complex than this. In cases of large velocity contrast such as the Tarim Basin region, there are multiple surface wave arrivals with a distinct arrival passing through the basin and another traveling around it. The arrivals merge at longer periods. Special care is required for construction and use of dispersion and attenuation models in such cases.

2 OVERVIEW

The importance of long period (>~10 second) surface waves for nuclear monitoring is in the discrimination capability of the M_s:m_b discriminant and its variants (Marshall and Basham, 1972; Stevens and Day, 1985). In general, contained underground explosions generate larger m_b relative to M_s than earthquakes of comparable size (Figure 1).

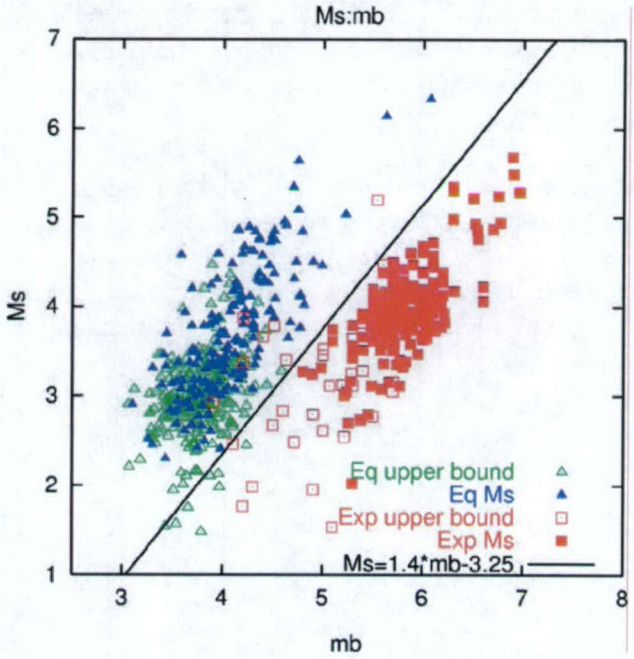

Figure 1. Explosions and earthquakes plotted on an Ms:mb diagram (from Stevens and McLaughlin, 2001). Open symbols are upper bounds on Ms.

M_s:m_b is one of the most reliable earthquake/explosion discriminants, but it has some limitations which we have tried to address in this study:

1. Body waves can be measured for significantly smaller events than surface waves, so the discriminant is not useful for very small events. We have addressed this issue by investigating methods to reduce the threshold for which surface waves can be reliably identified and measured, including development of improved dispersion maps constrained by a very large data set to facilitate phase-matched filtering.

2. While the strongest surface wave signals are at the closest distances, M_s is an unreliable amplitude measure at regional and local distances because of differences in dispersion and variations in the frequency content of the signal. We have addressed this issue by developing surface wave measurement techniques that can be used at local and regional distances, even very close to the source, which are consistent with measurements made at greater distances.

3. The discrimination capability of surface waves decreases with increasing frequency because the spectral difference between earthquakes and explosions declines. We have addressed this issue by analyzing surface wave signal and noise measurements to define the optimum frequency bands for discrimination.

4. Association of surface waves with the wrong event is a problem that can potentially lead to misclassification of an explosion as an earthquake. We have addressed this issue in two ways: first, by improving dispersion models that are used in the dispersion test for surface wave identification; and second by implementing and testing an improved azimuth estimation technique that can be used to improve association of surface waves with the corresponding event.

5. In general surface waves can be modeled quite well using path-averaged dispersion and attenuation calculated from discrete plane-layered earth models and great circle propagation, however there are some complex cases where standard methods of measuring surface wave dispersion and amplitude measurement do not work well. We have investigated some problem cases and made recommendations for techniques to handle these situations.

3 GLOBAL TOMOGRAPHIC INVERSION FOR EARTH MODELS AND DISPERSION MAPS

We develop global regionalized earth and dispersion models by inversion of a very large data set of phase and group velocity dispersion measurements. The data set has grown from about 90,000 (Stevens and McLaughlin, 2001) to over one million data points, and the resolution has improved such that the base model has changed from a 5 degree grid to a one degree grid. The dispersion measurements are inverted for earth structure, and the earth structure is then used to generate dispersion predictions as described below. The phase velocity dispersion curves are then used to calculate phase-matched filters to improve detection. An important advantage gained from using earth models is that we can include information from other studies leading to physically reasonable constraints on dispersion. For our earth models this information consists of the boundaries between geologic zones, bathymetry of oceans, thicknesses of sediments and ice, Moho depths, and prior estimates of seismic velocities derived from Crust 2.0 and AK 135 earth models. These constraints are important for filling in the gaps found in the path coverage of our data set and they enable dispersion prediction along paths with limited data.

3.1 Dispersion Data Set

The dispersion data set has been derived from a variety of regional and global studies including the following: global surface wave group velocities from earthquakes derived using IMS data (Stevens and McLaughlin, 1996), augmented with additional measurements derived from IMS data; surface wave phase and group velocity dispersion curves from underground nuclear test sites (Stevens, 1986; Stevens and McLaughlin, 1988), calculated from earth models for 270 paths (test site – station combinations) at 10 frequencies between 0.015 and 0.06 Hz; phase and group velocity measurements for western Asia and Saudi Arabia from Mitchell et al.(1996) for 12 paths at 17 frequencies between 0.012 and 0.14 Hz; the global phase velocity model of Ekstrom et al. (1996) for 9 periods between 35 and 150 seconds calculated for each grid block from a spherical harmonic expansion of order $l = 40$; group velocity measurements for Eurasia from Ritzwoller et al. (1996) and Levshin et al. (1996) for 20 frequencies between 0.004 and 0.1 Hz with 500 to 5000 paths per frequency; Antarctic and South American group velocity measurements from the University of Colorado (Vdovin et al., 1999; Ritzwoller et al., 1999); high frequency Eurasian dispersion measurements from University of Colorado (Levshin et al, 2003); dispersion measurements from Central Asia made by Los Alamos National Laboratory (Yang et al, 2002); data from China (Huang et al, 2003); and data from the New Madrid region from Mancilla (2001).

Figure 2 shows the frequency distribution of group velocity and phase measurements in our data set, excluding the phase velocities derived from the global phase velocity model of Ekstrom et al. (1996). Figure 3 shows the geographic distribution of data coverage. Coverage is excellent in Eurasia for all frequencies, and good in most continental regions at 20 seconds and lower. Data coverage is more limited in the oceans, particularly at higher frequencies. The maps show "hit densities," in log10 scale, over the one degree cells for all group velocity measurements in the data for the indicated frequency ranges. The density for each cell is the sum of proportions of the lengths to total lengths of all paths passing through the cell. So, for example, a hit density of 10 could mean that 100 rays, each 10 degrees in length, pass through the cell.

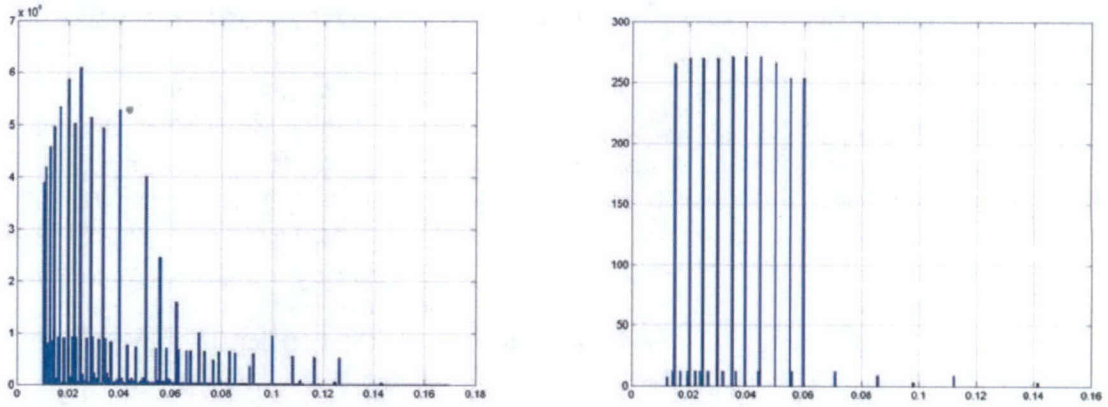

Figure 2. Bar graph of the number of group velocity measurements (left) and phase velocity measurements (right) in each frequency band for data currently used in the tomographic inversions.

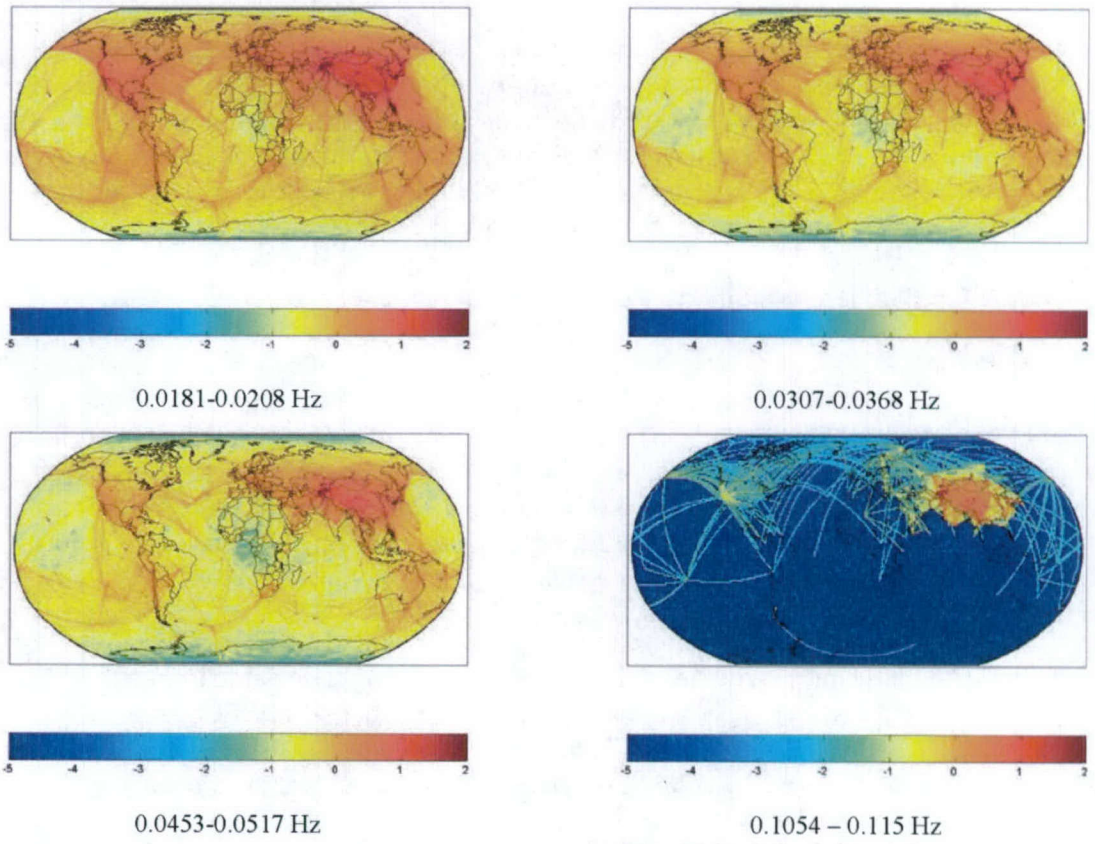

Figure 3. Distribution of group velocity data at 50 seconds (top left), 30 seconds (top right), 20 seconds (lower left) and 10 seconds (lower right). The maps show hit densities in log10 scale for each one degree cell. Red indicates a high density of coverage with many rays crossing each cell. Dark blue indicates little or no data.

3.2 Global Earth Models and Dispersion Models

The regionalized earth model consists of 1°x1° blocks and is made up of layers of ice, water, sediments, crust and upper mantle. This model depends on 9022 free parameters which are adjusted by a damped least squares fit to Rayleigh wave dispersion data. The free parameters are the S-wave velocities of layers of 577 different model types. Other constrained parameters in the model are P wave velocities, densities and Q. The model types are based on the Crust 2.0 2°x2° crustal types (Bassin et al., 2000 and Laske et al. 2001) and also on ocean ages (Stevens and Adams, 2000). The top few km of the model (consisting of water, ice and/or sediments) are fixed and match data from one degree bathymetry maps made by averaging Etopo5 five minute measurements of topography, and Laske and Masters (1997) 1 degree maps of sediments. There is an explicit discontinuity between the bottom of the sediments and the crust. There are three or more crustal layers. The Crust 2.0 models, which were the starting point for these structures, have three crustal layers, but we found it necessary to add more layers in regions of thick crust. There is another explicit discontinuity at the Crust/Mantle boundary. The Moho depth is derived from Crust 2.0 and varies on a 2° grid. The mantle starting model is derived from AK135 (Kennett, et al, 1995). With these constraints, the inversion is performed for the shear velocity of the crust and upper mantle to a depth of 310 km. Below 310 km the earth structure is fixed, and the inversion model is required to be continuous with the mantle structure at the base of the inversion. In broad ocean areas, we replace the Crust 2.0 model with models distinct for each ocean and subdivided by ocean age. We also separate into distinct models Crust 2.0 models that are geographically separated. So, for example, if Crust 2.0 has the same model type in North America and in Asia, we use the same starting model for each, but treat them as separate models in the inversion.

3.3 The Inversion Procedure for the 3D Earth Model

The relationship between dispersion and the shear wave velocities of the layers in the earth model is non-linear, so the shear velocities are estimated by an iterative least squares inversion procedure. At each step a system of tomographic equations is formed, augmented by additional equations of constraint, and then solved by the LSQR algorithm. The equations solved are

$$\begin{pmatrix} A \\ sH \\ \lambda I \end{pmatrix} \vec{\Delta x} = \begin{pmatrix} \vec{\Delta d} \\ -sH\vec{x} \\ \lambda\left(\vec{x}_C - \vec{x}\right) \end{pmatrix} + \vec{\varepsilon} \quad , \tag{3.1}$$

where $\Delta\mathbf{x}$ is the vector of adjustments to the shear wave slownesses of layers in each of the 577 model types. $\Delta\mathbf{d}$ is the vector of slowness differences between predicted and observed dispersion measurements. $\boldsymbol{\varepsilon}$ is the vector of residuals that remain after inversion (the inversion minimizes $|\boldsymbol{\varepsilon}|^2$). $\mathbf{x}$ is the vector of slownesses estimated in the previous iteration. The elements of the matrix $\mathbf{A}$ consist of partial derivatives of dispersion predictions with respect to shear wave slownesses in each layer. $\mathbf{H}$ is a difference operator that applies to vertically neighboring layers and has the effect of constraining the vertical smoothness of velocity profile. $\mathbf{H}$ applies to layers in the crust and upper mantle, but has explicit discontinuities at the crust/mantle boundary and at the base of surface sediments. $\mathbf{s}$ is the weighting of the smoothness constraint and can be a diagonal matrix (for variably weighted smoothing) or a scalar (constant smoothing). A different smoothing

parameter can be selected for each model type. Lateral smoothing, which is usually applied in tomography studies, is executed indirectly in our study through selection of the model types. **I** is the identity matrix and λ weights the damping which constrains the norm of the difference between final slownesses and constraining model slownesses $\mathbf{x}_c$ (in this case a variant of the Crust 2.0 values). λ can be a scalar for constant damping, or a diagonal matrix for variable damping. As with smoothing, variable damping is implemented so that a different parameter can be selected for each model type.

An important feature of Equation 3.1, and what makes this procedure different from most other tomographic inversion studies, is that we invert all relevant data in the same inversion. The data includes phase velocity and group velocity measurements measured along specific paths at all frequencies, as well as some phase and group velocity data points derived from models (e.g. the Harvard phase velocity models). It is also possible to include earth models as data, so that earth models from existing studies can be included in the inversion.

3.4 Regularization and Data Fit

The damping and smoothing constraints and their associated weighting parameters are used to regularize the solution. Regularization acts both to control the influence of data noise on the estimation of model parameters and to constrain parts of the model that are poorly constrained by data. Too much regularization will make the model too smooth, degrading the data fit, and too little regularization will allow noise to be projected into the model, making it unrealistic and rough. Techniques for optimization of regularization parameters are not yet mature, especially for large-scale problems such as this. The methods most often used (e.g. Hansen, 1998) are the L-curve, generalized cross validation, and discrepancy principle. We have experimented with several of these techniques for our inversion problem, but have not found any reliable enough to replace analyst review of the inversion results.

3.5 Identification of Data Problems and Improvements to Data Quality

The quality of the inversion results is limited by the quality of the data. Redundancy in the data helps to average out errors; but as the models improve, the remaining errors in the data begin to limit the improvement that is possible. Consequently, we initiated a review and assessment of the data quality, and made an effort to identify and remove data problems. This has made dramatic differences in the results in some areas. Some of the types of problems that we identified are:

1. Consistent errors made by research groups. In reviewing data sets, we find that they often contain consistent errors throughout the data set, most commonly errors in dispersion at either the high frequency or low frequency end of the dispersion curves. These errors can be identified by comparison with dispersion curves from other sources, and the problem data range can be removed.

2. Errors in location. Particularly on short paths, event location errors can lead to large errors in dispersion curves. If we have information about the event used to derive the dispersion curve, and a new, better location, then we can correct the error. We found, for example, that recalculating group velocities using improved locations from Engdahl et al (1998) greatly improved the consistency of the data.

3. Grazing paths along low velocity zones. This is a particularly troubling problem, because surface waves along these paths often show two distinct or interfering arrivals, one that travels through a low velocity basin and one that travels around it. Analysts may pick one or the other inconsistently. The problem can be reduced by ordering the arrivals such that the dispersion picks change from fast to slow to fast smoothly as the azimuth changes across the basin (see Section 5 of this report).

3.6 Prediction Statistics for One-Degree Earth Model

We evaluate the performance of the one-degree earth model for predicting dispersion in two ways: 1) by calculating the mean and standard deviation of the data residual for the entire data set, and 2) by comparing the residual error in the prediction vs. data with the consistency of the data set itself.

The means and standard deviations of normalized group velocity residuals, $1-v_o/v_p$, where v_o and v_p are observed and model predicted group velocities, were calculated for narrow frequency bands and are shown in Figure 3.3. The solid line is for our best 1-degree model, and dashed is for the best 5-degree model (Stevens and Adams, 2000) based on Crust 5.1 (Mooney, et al., 1998). Figure 4 shows the value of the 1-degree model, especially for high frequencies. We note, however, that the five degree model was based on a smaller data set and the performance would be better if a new inversion was performed with the complete, current data set.

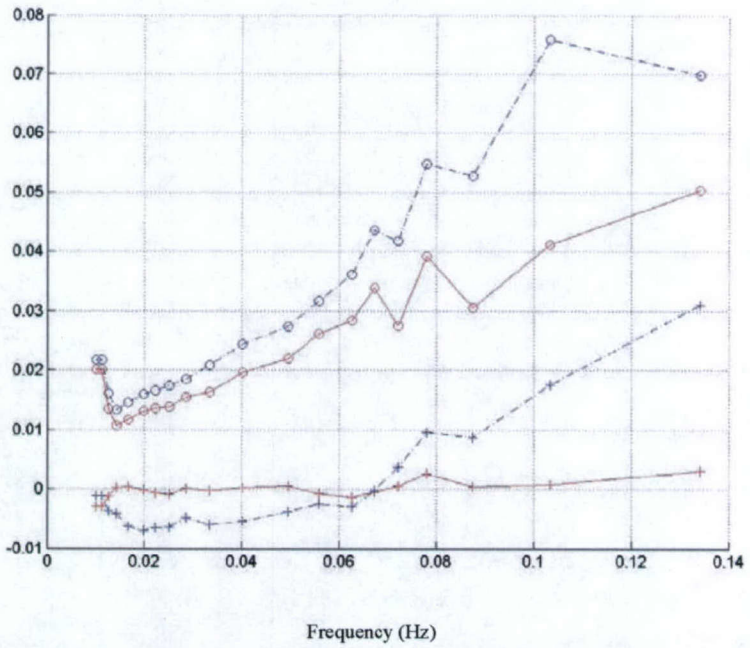

Figure 4. Standard deviations (o) and means (+) of normalized group velocity residuals are plotted against frequency for 1degree earth model (solid red) and 5-degree earth model (dashed blue).

As earth models have improved through the course of this project, improvement in models has become more limited by the accuracy of the data. Figure 5 illustrates estimates of data error together with residuals from the model. Sets of "master" paths were selected that each had 14 or more rays from different events and/or stations along very similar paths. Each path contains a bundle of rays within a "distance" of .01 of a "master" path. The distance is (d1+d2)/D where D is the length of the master path, and d1 and d2 are the distances between pairs of end points. These figures show that the data residuals are comparable to the errors in the data, and that further improvement in data quality has the potential to reduce data errors and allow further improvements in model prediction.

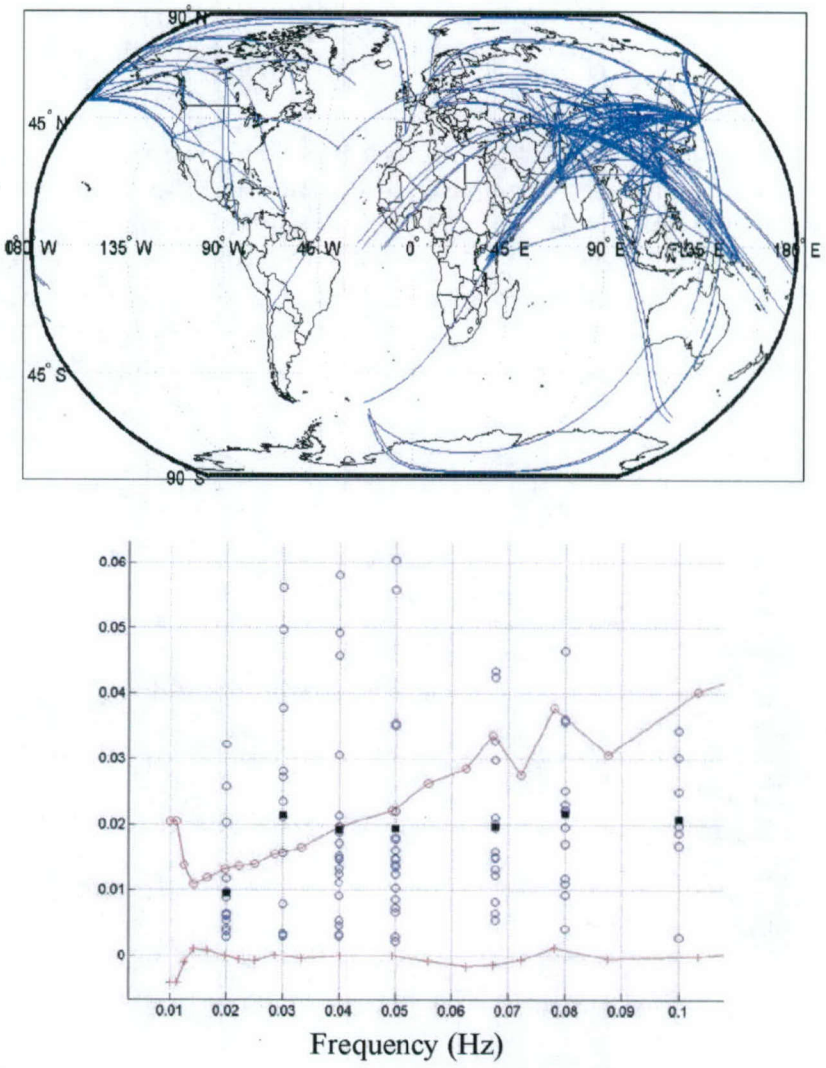

Figure 5. Comparison of model misfit and data error. The top figure shows a map of sets of closely spaced paths, each containing a bundle of at least 14 rays. The b figure shows data residuals relative to the model (red, + are averages and o standard deviations) and standard deviations of the measurements along similar paths (blue). Black squares are the mean of the standard deviations at the same frequency.

3.7 Surface Wave Amplitude Predictions from Global Earth Models

Surface wave amplitudes can be predicted with an approximation originally due to McGarr (1969) that uses propagation of surface waves along great circle paths with conservation of energy across material interfaces and no mode conversion. With these approximations, surface wave propagation in a heterogeneous, anelastic structure takes the following form, separating source, path and receiver (notation follows Harkrider et al, 1994):

$$u_z(\omega,r,\varphi)=\frac{1}{\sqrt{a_e\sin(r/a_e)}}\sqrt{\frac{2A_{R_1}}{\pi\omega c_1^{\,2}}}\sqrt{c_2A_{R_2}}\exp\left[i\left(\pi/4-\omega r/c_p-\gamma_p r\right)\right]F_s(\omega,\varphi,h) \qquad (3\text{-}2)$$

where ω is angular frequency, r is source to receiver distance, a_e is the radius if the earth, φ is azimuth, A_R is the Rayleigh wave excitation function, c is phase velocity, γ is the attenuation coefficient, and the subscripts *1*, *2*, and *p* refer to parameters derived from the source region structure, parameters derived from the receiver region structure, and parameters which are defined by path averages, respectively. All source properties are contained in the function F_s. For an isotropic explosion source, the Rayleigh wave spectrum can be written:

$$u_z(\omega,h_x,r)=M_0^{'}\frac{S_1^x(\omega,h_x)S_2(\omega)\exp[-\gamma_p(\omega)r+i(\varphi_0-\omega r/c_p(\omega))]}{\sqrt{a_e\sin(r/a_e)}} \qquad (3\text{-}3)$$

where φ_0 is the initial phase equal to -3π/4, S_1^x depends on the source region elastic structure and the explosion source depth, h_x depends on the receiver region elastic structure. $M_0^{'}=\frac{3\beta^2}{\alpha^2}M_0$ where M_0 is the explosion isotropic moment. $M_0^{'}$ is defined this way so that the function S_1^x does not depend explicitly on the material properties at the source depth. (More details are given in Stevens and McLaughlin (2001) and Stevens and Murphy (2001)).

3.8 Properties of the One-degree Earth Model

In this section we show the values and distribution of quantities derived from the one-degree earth model. Figure 6 shows group velocity as a function of frequency for all models, and Figure 7 shows a map of group velocity at 50 and 20 seconds.

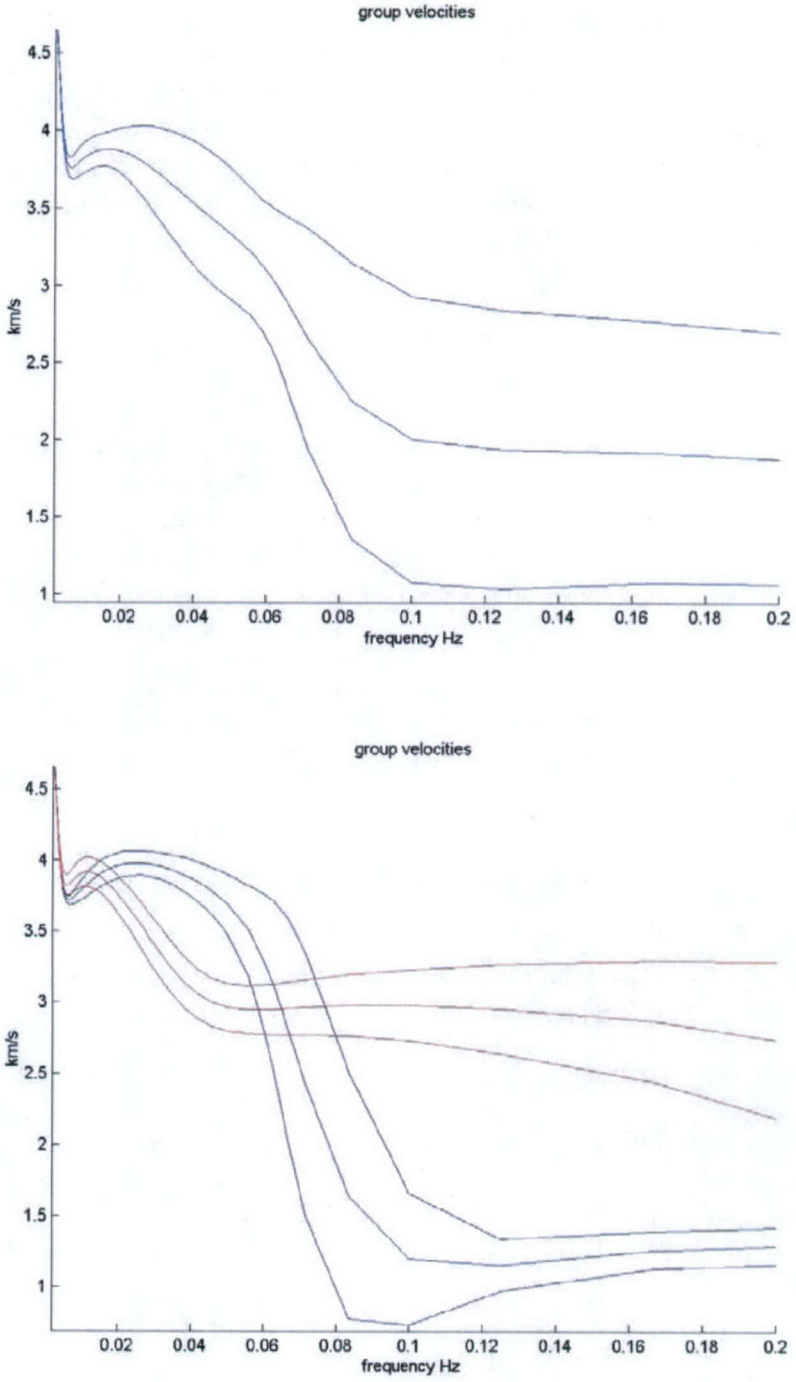

Figure 6. Average group velocity plotted vs. frequency and ± one standard deviation. Top figure is for all earth models. Bottom figure shows continental models (red) and oceanic models (blue).

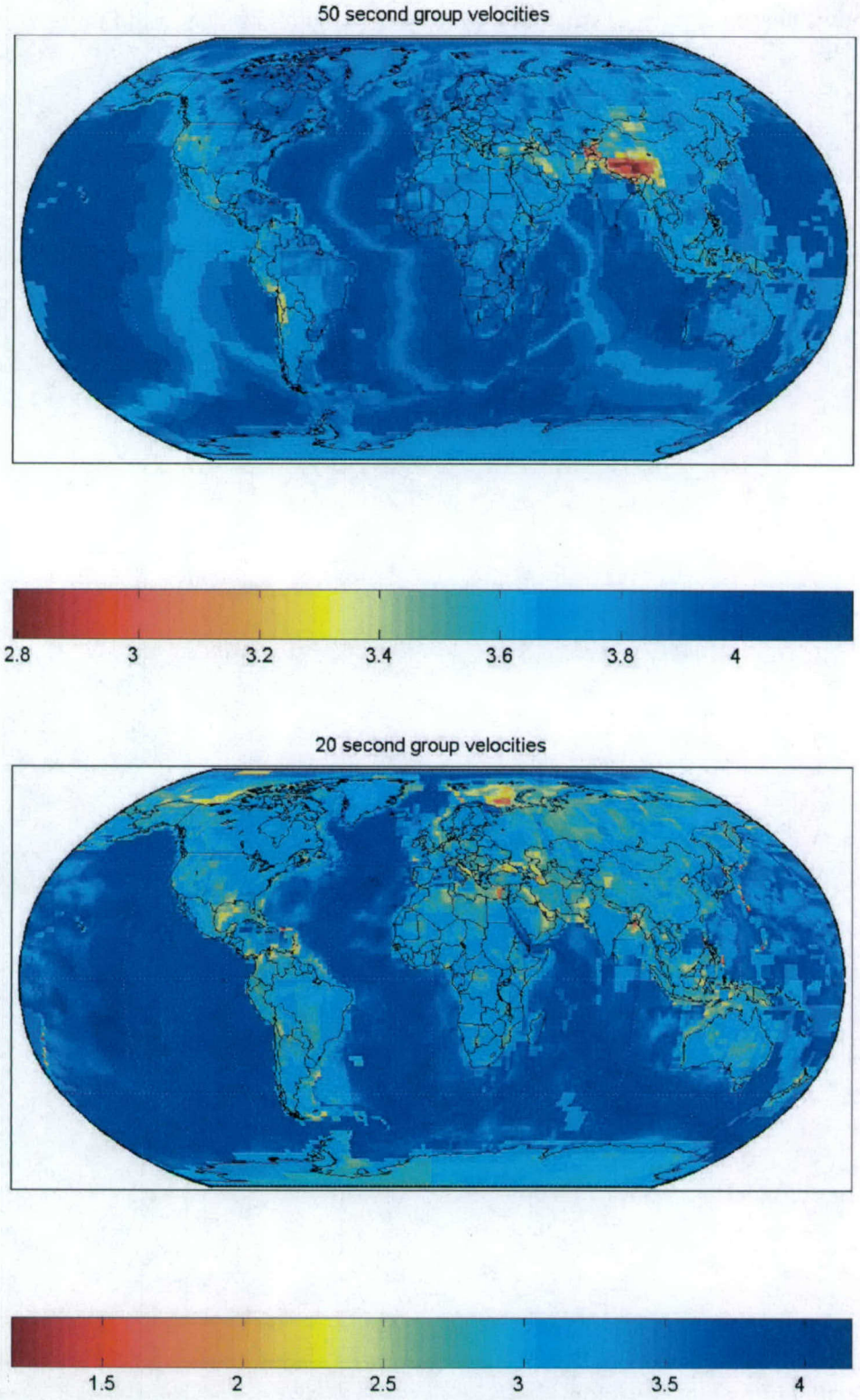

Figure 7. Map of group velocities at 50 seconds (top) and 20 seconds (bottom).

Figure 8 shows phase velocity as a function of frequency for all models, and Figure 9 shows a map of phase velocity at 50 and 20 seconds.

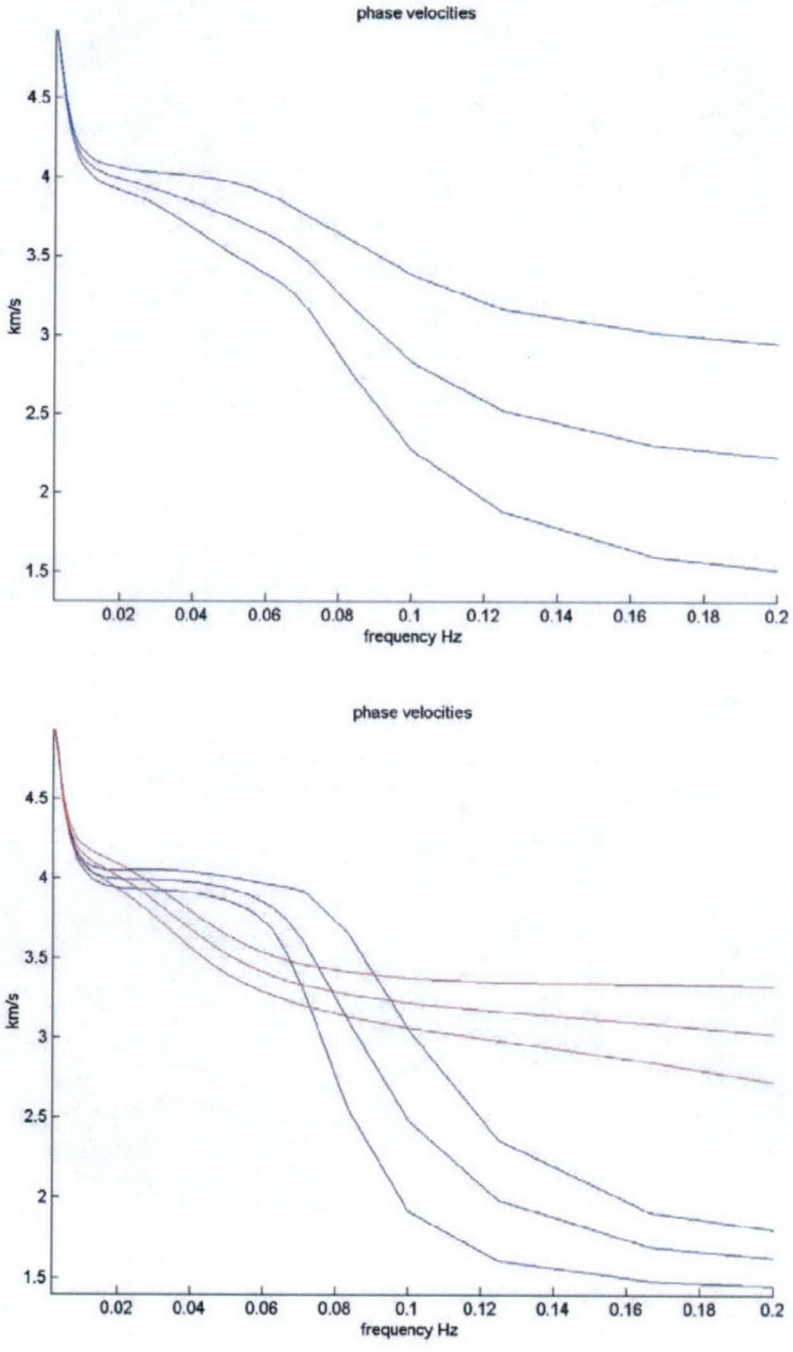

Figure 8. Average phase velocity plotted vs. frequency and ± one standard deviation. Top figure is for all earth models. Bottom figure shows continental models (red) and oceanic models (blue).

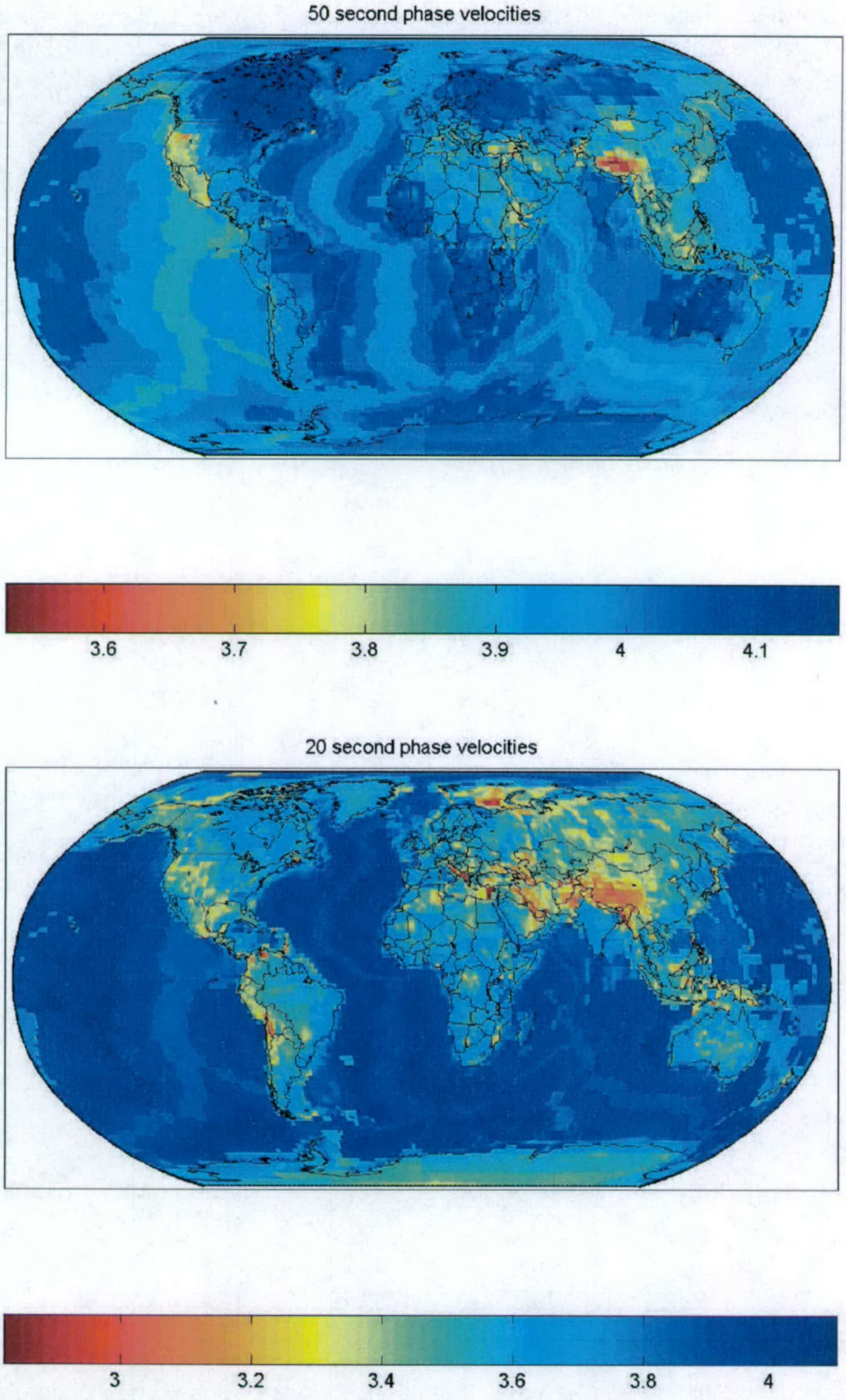

Figure 9. Map of phase velocities at 50 seconds (top) and 20 seconds (bottom).

Figure 10 shows the attenuation coefficient, gamma, as a function of frequency for all models, and Figure 11 shows a map of gamma at 50 and 20 seconds. The attenuation coefficient is derived from generic models, not through inversion of attenuation data, so should be regarded as approximate.

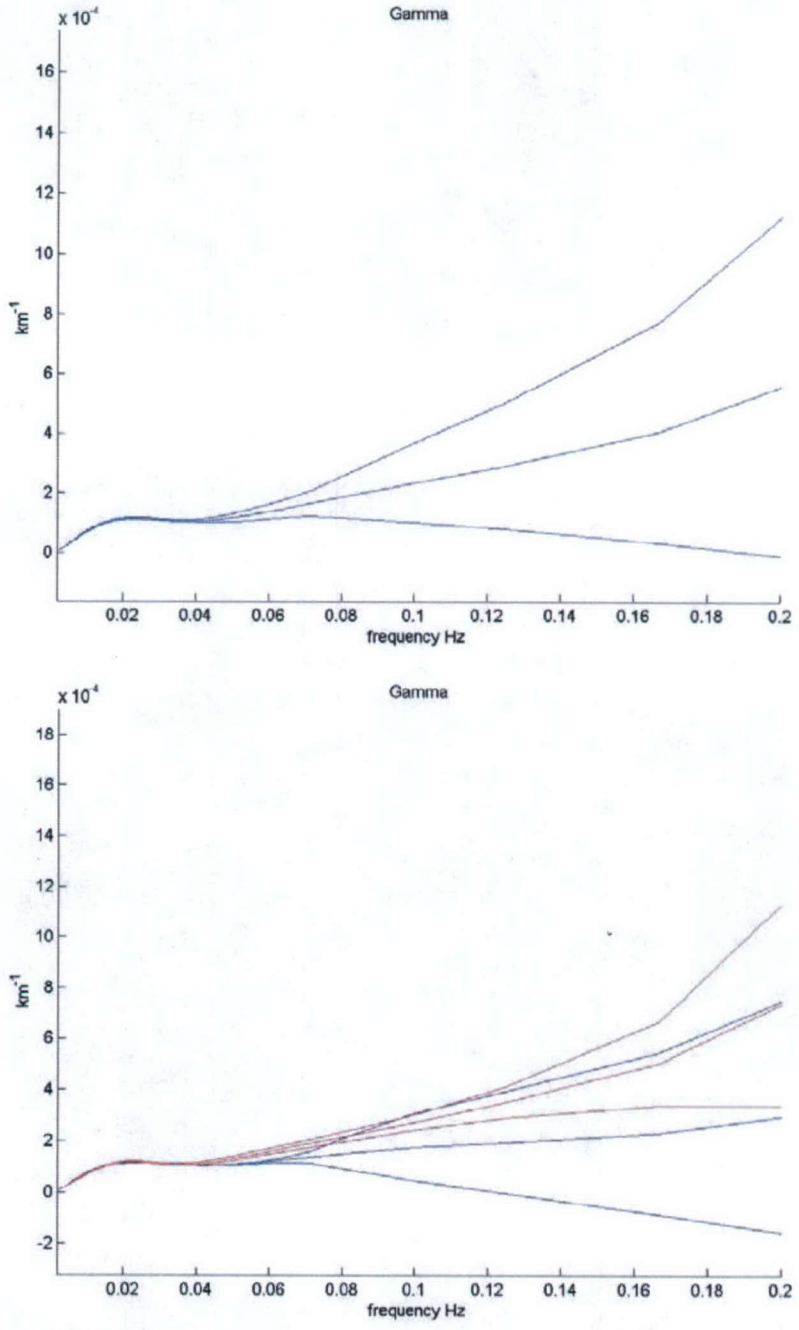

Figure 10. Average attenuation coefficient plotted vs. frequency and ± one standard deviation. Top figure is for all earth models. Bottom figure shows continental models (red) and oceanic models (blue).

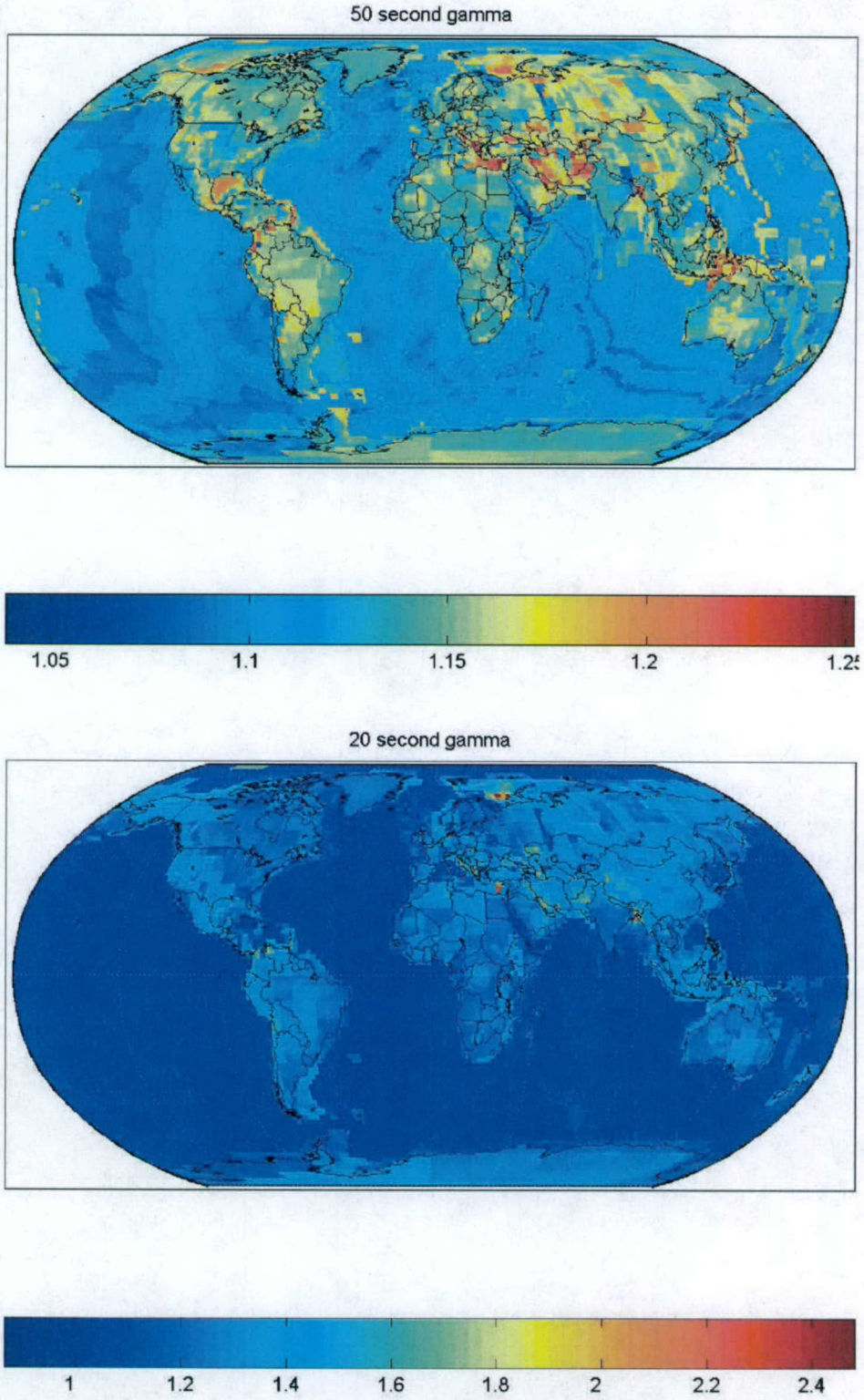

Figure 11. Map of gamma at 50 seconds (top) and 20 seconds (bottom).

Figure 12 shows the source region excitation function, S1, as a function of frequency for all models, and Figure 13 shows a map of S1 at 50 and 20 seconds.

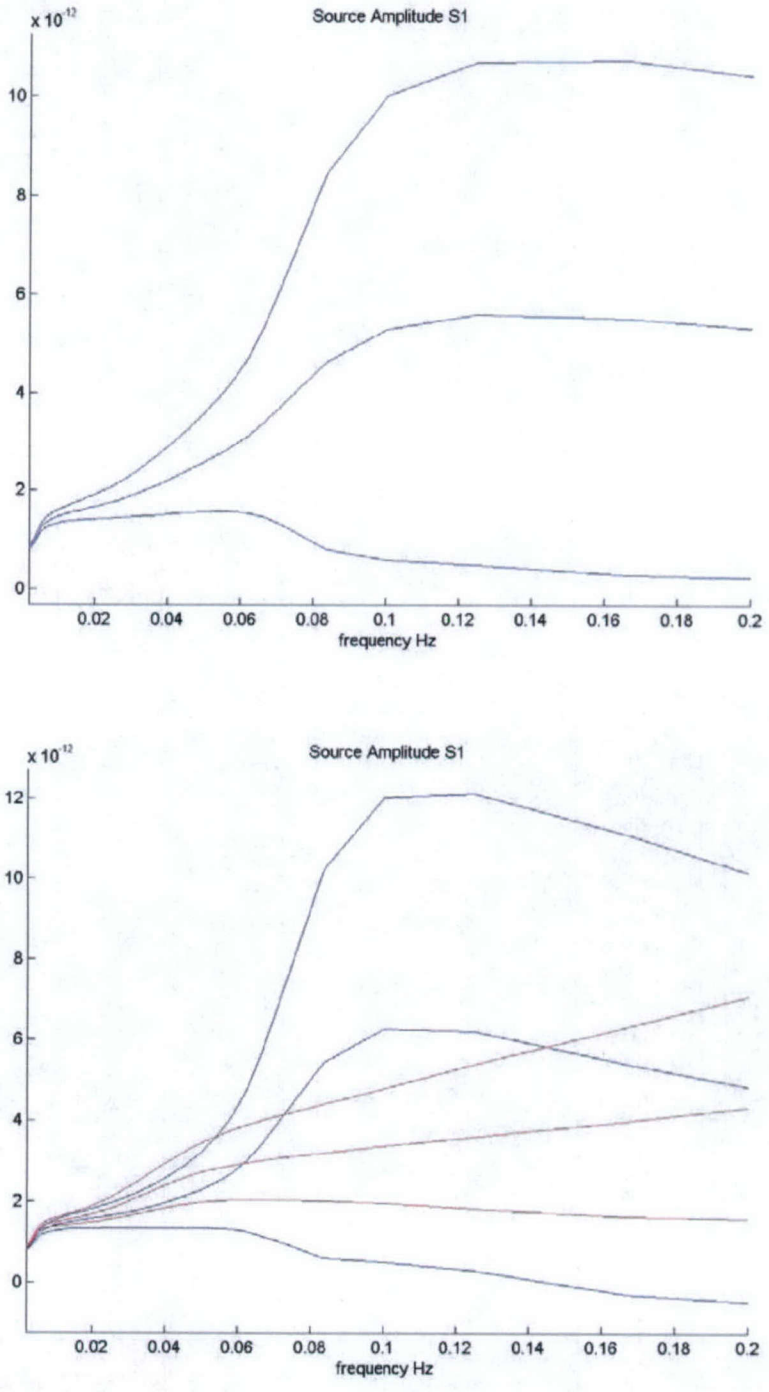

Figure 12. Average source amplitude, S1, plotted vs. frequency and ± one standard deviation. Top figure is for all earth models. Bottom figure shows continental models (red) and oceanic models (blue).

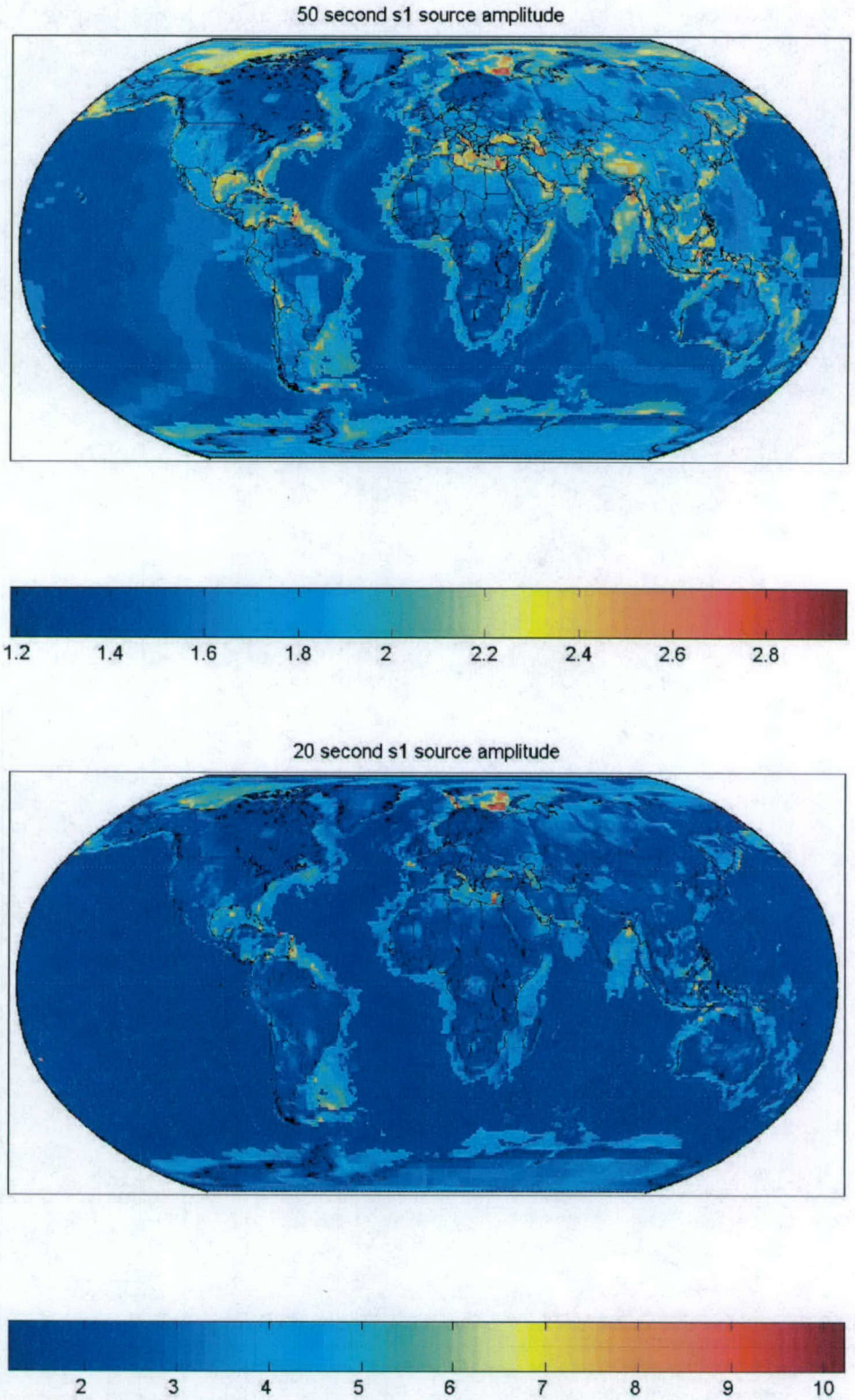

Figure 13. Map of S1 at 50 seconds (top) and 20 seconds (bottom).

Figure 14 shows the receiver region amplitude function, S2, as a function of frequency for all models, and Figure 15 shows a map of S2 at 50 and 20 seconds.

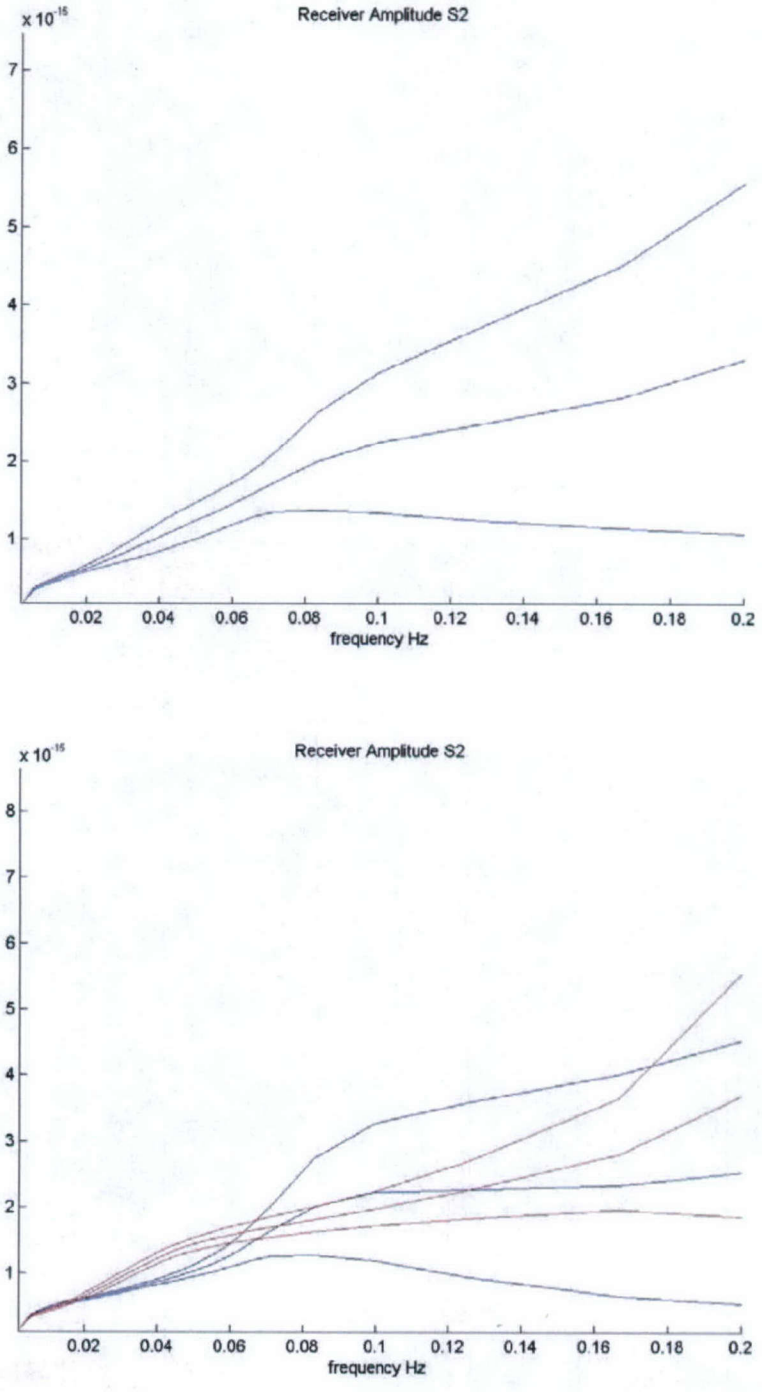

Figure 14. Average source amplitude, S2, plotted vs. frequency and ± one standard deviation. Top figure is for all earth models. Bottom figure shows continental models (red) and oceanic models (blue).

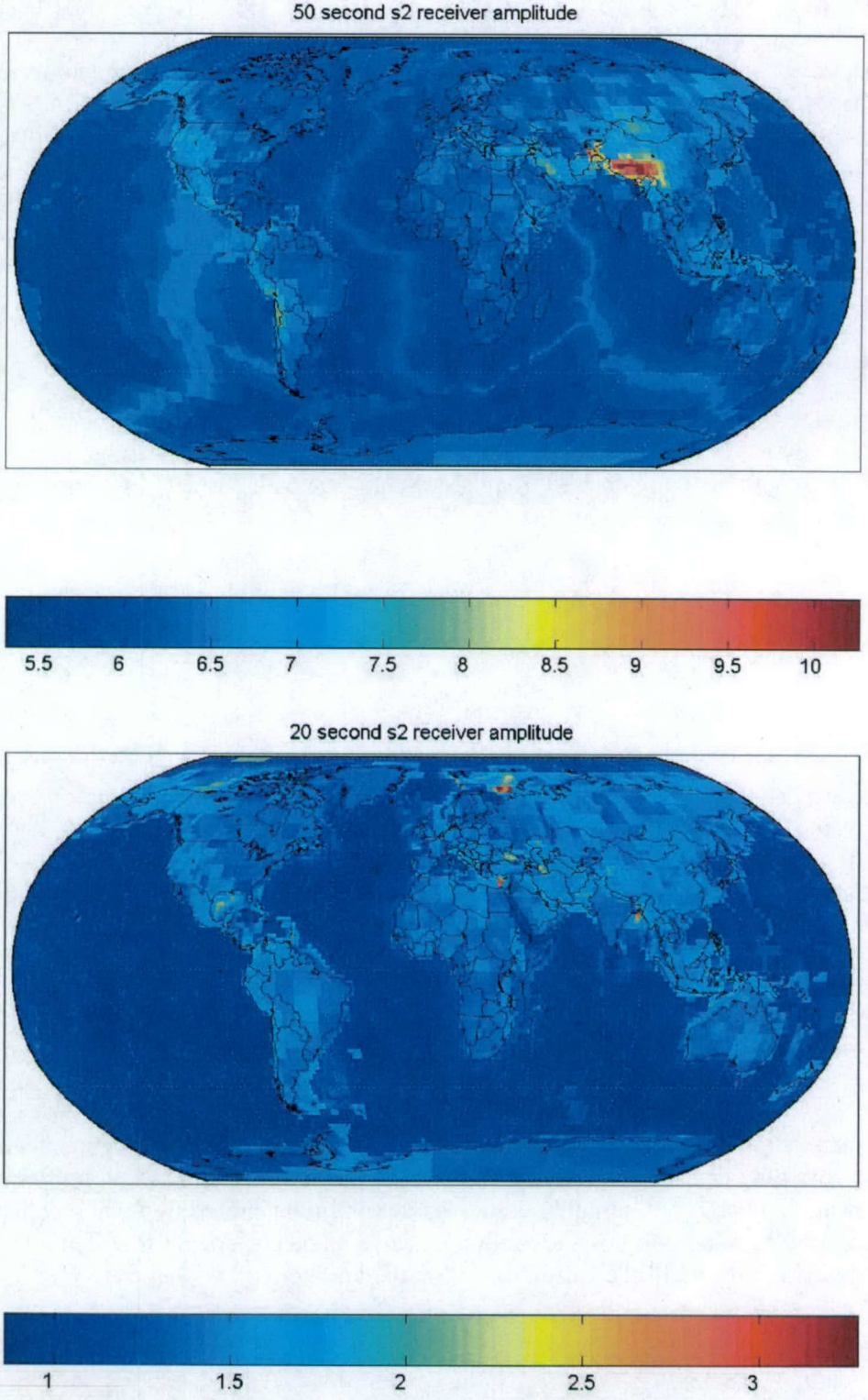

Figure 15. Map of S2 at 50 seconds (top) and 20 seconds (bottom).

4 OPTIMIZED SURFACE WAVE AMPLITUDE MEASUREMENTS

Surface wave measurements traditionally are accomplished by measuring a time domain amplitude at a period near 20 seconds and then calculating a surface wave magnitude M_s. This procedure is problematic at regional distances because the surface wave is not well dispersed and a distinct 20-second arrival may not be present. It is possible to measure time domain amplitudes at higher frequencies with corrections (e.g. Marshall and Basham, 1972), however measurements may be inaccurate due to differences in dispersion caused by differences in earth structure. Stevens and McLaughlin (2001) suggested as an alternative replacing time domain measurements with a path corrected spectral magnitude.

4.1 Path Corrected Spectral Magnitudes

The path corrected spectral magnitude, $\log M_0$, is calculated by dividing the observed surface wave spectrum by the Green's function for an explosion of unit moment and taking the logarithm of this ratio, averaged over any desired frequency band. The path corrected spectral magnitude is defined as the logarithm of:

$$M_0' = \left| U(\omega, r, \theta) \Big/ \left(\frac{S_1^x(\omega, h_x) S_2(\omega) \exp[-\gamma_p(\omega) r]}{\sqrt{a_e \sin(r/a_e)}} \right) \right| \tag{4.1}$$

where U is the observed surface wave spectrum, and as described earlier S_1^x depends on the source region elastic structure and the explosion source depth, S_2 depends on the receiver region elastic structure, γ_p is the attenuation coefficient that depends on the attenuation integrated over the path between the source and receiver, r is the source to receiver distance and a_e the radius of the earth. All of the functions in equation 4.1 are easily derived from plane-layered earth models, and allow the measurement to be regionalized to account for differences in earth structure at the source and receiver, and due to attenuation along the path.

The advantages of using $\log M_0$ instead of the traditional surface wave magnitude M_s are that $\log M_0$ is insensitive to dispersion, independent of distance, works well at regional distances, and can be regionalized. Regionalized path corrected spectral magnitudes incorporate geographic variations in source excitation and attenuation. Furthermore, as discussed below, it can in principle be measured over different frequency bands to optimize the signal-to-noise ratio. M_s and $\log M_0$ share some limitations: spectra from earthquakes vary due to source mechanism and depth, and errors can occur if the measurement is made in a spectral dip or at high frequencies for a deep event (Figure 16). Azimuthal variations in amplitude caused by focal mechanism also affect the amplitudes of both $\log M_0$ and M_s. $\log M_0$ can also be corrected for structural heterogeneity using the amplitude corrections described earlier.

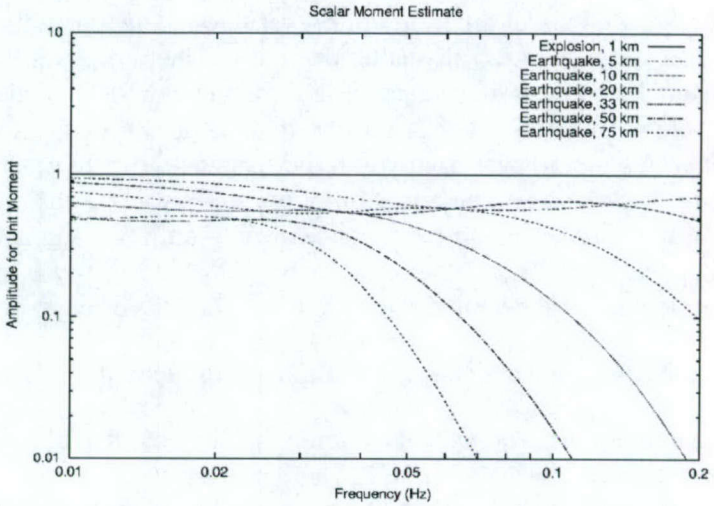

Figure 16. Path corrected spectra for an explosion and for earthquakes calculated for several depths. The path corrected explosion spectrum is flat over the entire frequency band (for perfect data and path correction), while the path corrected earthquake spectrum is flattened, but has some variation due to source mechanism and source depth.

The test cases discussed by Stevens and McLaughlin (2001) used a frequency band of 0.02-0.05 Hz (50-20 second period) to estimate the spectral magnitudes. They estimated that on average, the time domain and spectral magnitudes are related as $\log M_0 = M_s + 11.75$. Most of the waveforms in that work were recorded at distances exceeding 8°. Due to the relatively flat path corrected spectra over the 0.02-0.05 Hz band for most data, this choice worked quite well. The authors noted, however, that higher frequencies might be required for shorter paths. An important observation was that the $\log M_0$ residuals are independent of distance, despite the simple Q models used in the earth structures (Figure 17).

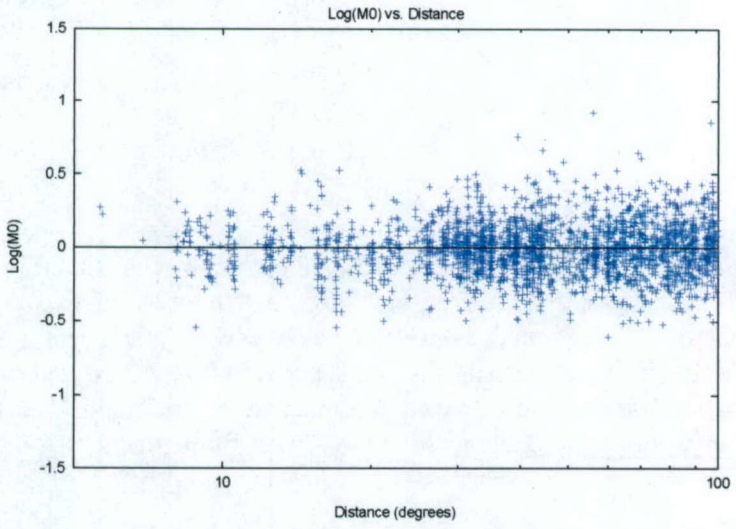

Figure 17. Path corrected spectral magnitude (Log M_0) residuals plotted vs. distance (from Stevens and McLaughlin, 2001). Log M_0 is nearly independent of distance.

In the following test case, we look at the utility of higher frequencies for estimating spectral magnitudes of smaller events, recorded at smaller distances. The purpose is to optimize the spectral magnitude estimates, to test their distance and frequency independence, and to identify any measurement problems or pitfalls. For large amplitude signals we can expect the lower frequencies to be better in general, particularly at larger distances due to greater attenuation at higher frequencies. Our hypothesis at the initiation of the study was that using higher frequencies for measuring spectral magnitudes at shorter distances would optimize signal to noise ratio and therefore be better for measuring surface waves at regional distances, however as discussed below this is only true to a limited extent and may come at the cost of degraded discrimination.

4.2 Surface Wave Measurements Using Events On and Near the Lop Nor Test Site

To optimize the measurement procedures and examine the performance of the path corrected spectral magnitude at regional distances, we used 584 spectra from 76 earthquakes and 11 explosions in the Lop Nor area (Figure 18). Approximately 11% of the spectra used for the $\log M_0$ estimates originate from records at source-station distances of 5° or less, and another 11% at distances of 30° or greater. The bulk of the data comes from intermediate distances.

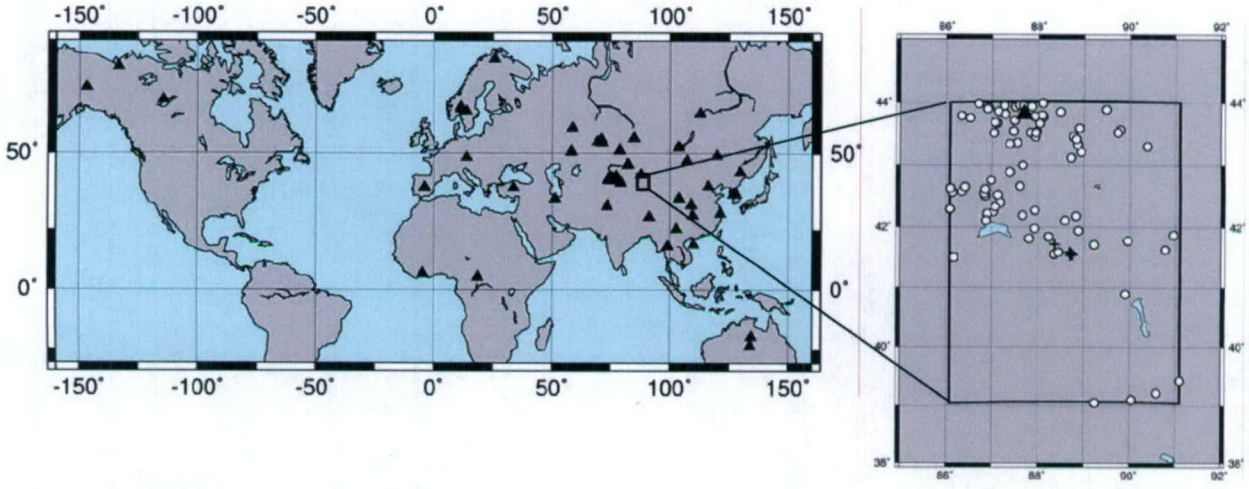

Figure 18. Maps showing the Lop Nor area (rectangle), stations (triangles), and earthquake (circles) and explosion (crosses) epicenters.

Figure 19 shows examples of explosion and earthquake path corrected spectra from Lop Nor at various distances. The explosion spectra are flattened as expected, while there is more variation of the earthquake spectra with frequency. This happens because 1) the spectra are corrected by an explosion Green's function that flattens earthquake spectra imperfectly, and 2) the earthquake spectra have frequency variations caused by source mechanism and depth. Most of the spectra shown in Figure 19 are contaminated by noise at the lowest frequencies.

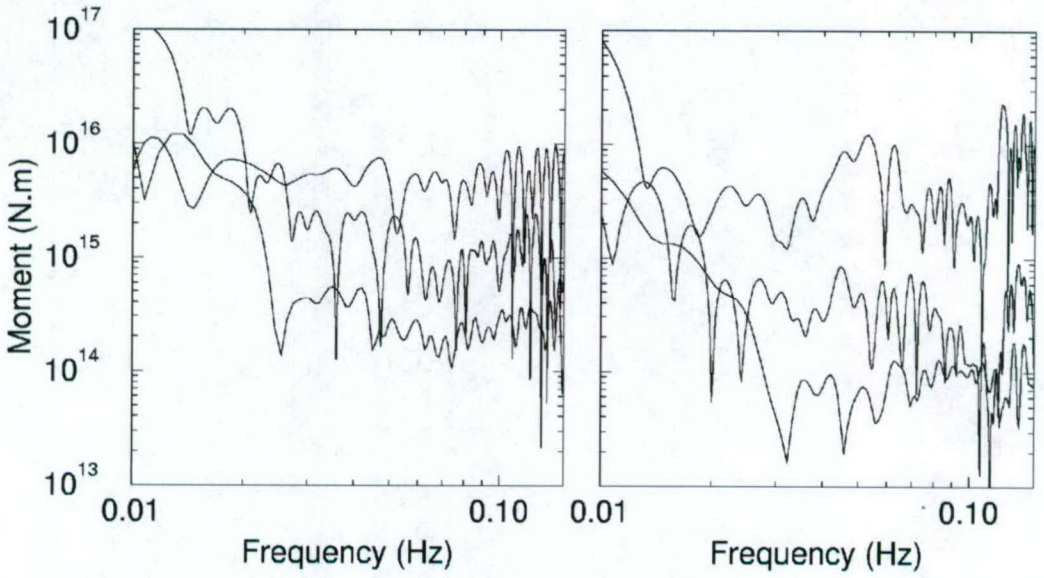

Figure 19. Examples of path corrected spectra used in this work: (a) Lop Nor explosions recorded at distances of 2°, 7° and 67° (left); (b) Lop Nor earthquakes recorded at distances of 0.4°, 22° and 65° (right). See examples of station logM_0 estimates in Table 1. S/N is good at all but the highest frequencies. Low frequency noise dominates over the surface wave signal below about 0.02 Hz.

We calculated individual spectral magnitudes (i.e., several station magnitudes per event) over all possible frequency bands between 0.02 Hz (50 s) and 0.15 Hz (~7s), with bandwidths of 0.03 Hz, 0.04 Hz, etc., up to 0.13 Hz for the 0.02-0.15 Hz band. This procedure provided 153 bands to examine from each spectrum. Four different methods were used as follows to identify the most robust spectral magnitude estimate.

1. Calculating a "simple" mean of the logarithms of all path corrected amplitude measurements made in a given frequency band. This is comparable to Stevens and McLaughlin's (2001) estimates in the 0.02-0.05 Hz band.

2. Iteratively calculating a "robust" mean, by rejecting outliers outside two standard deviations from the mean calculated at each step. The procedure ends when all measurements remain within two standard deviations or when half of the amplitude measurements in a frequency band are rejected, whichever occurs first. Thus the spectral magnitude estimates are much less affected adversely by the tendency of some spectra to sharply vary in amplitude over some frequencies, with most outliers marking anomalously low amplitudes (see Figure 19 above). Figure 20 compares the individual (station) logM_0 estimates from (1) and (2). Standard deviations from the robust-mean method are predictably lower than those in the simple-mean method, as the insets in Figure 20 show.

3. Calculating logM_0 at the center frequency of a least-squares straight line fit to the spectrum over a given frequency band.

4. Same as (3), but the straight line is "robust", minimizing the absolute deviations of the logarithms of the amplitudes from the line.

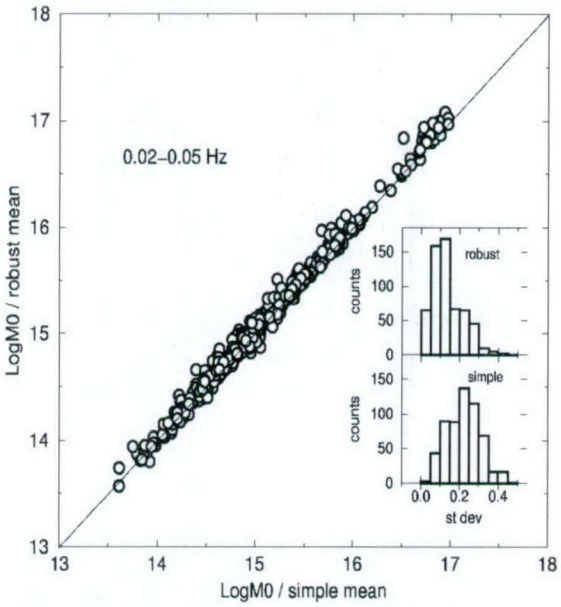

Figure 20. Comparison of station spectral magnitudes calculated with two different methods. Insets show standard deviations as indicated. See text for details.

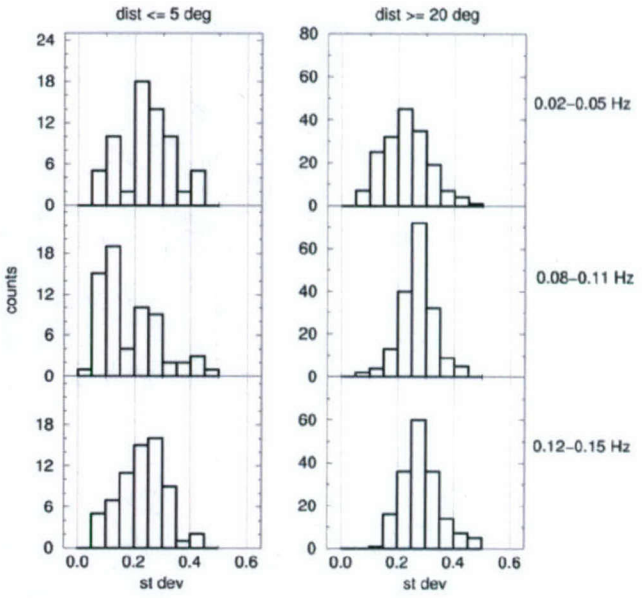

Figure 21. Histograms of standard deviations of the mean station $\log M_0$ estimated in three frequency bands (shown on right), for small and larger distances (shown on top).

The above estimates were compared in order to select the most suitable frequency bands, possibly varying with distance. Ideally, the corrected spectra would be flat over an extended band of frequencies. Flatness is particularly expected for explosions, as supported (within limits) by the explosion examples in Figure 19 above. The magnitude spectra estimated over any reasonable band would be then consistent. In reality, completely flat spectra over extended frequency bands are rare, so we need to choose bands small enough not to include too many variable features of the spectra, yet large enough not to reflect only local, possibly spurious, characteristics.

In view of the above, the two main desirable properties of a spectrum over a given frequency band are small standard deviations and flatness. For this reason, in our search for optimum frequency bands we used two criteria. First, small standard deviations from (1) above represent one measure of the suitability of a frequency band. Figure 21 indicates that for small distances, the 0.08-0.11 Hz frequency band may be preferable (the largest number of small standard deviations) to either 0.02-0.05 Hz, or 0.12-0.15 Hz. Larger distances do not present a clear picture, but it is still evident that relatively more small standard deviations are found in the 0.02-0.05 Hz frequency band, compared with the higher frequencies. We note that at this stage we do not use the standard deviations from (2), since they are designed to greatly diminish the presence of outliers and are thus not representative enough of the quality of the estimates in the different frequency bands. However, once a suitable frequency band is chosen, the robust mean is the most reliable estimate of $\log M_0$. Spectral flatness as measured with the slopes of the "robust" lines in (4) above provides a second measure of the quality of frequency band; the smaller the slope, the flatter the spectra. Table 1 shows examples of selected estimates, over one specific

frequency band out of 153 (0.05-0.1 Hz), for the explosion and earthquake spectra shown in Figure 19. Smaller slopes (flatter spectra) are evident for explosions compared with earthquakes. On the other hand, increasing absolute values of slopes and standard deviations are seen for earthquakes with increasing distance. This is to be expected, as the relatively high-frequency band in the example is less suitable as distance increases.

Table 1. Station LogM0 estimates in 0.05-0.10 Hz from the spectra in Figure 19.

Event Type	*ID.station*	*Distance, degrees*	*Station $logM_0$ (simple)*	*Station $logM_0$ (robust)*	*Station slope/$logM_0$*	m_b
Explosions	21450528.WMQ	2.2	14.31+0.10	14.33+0.08	+1.02/14.31	4.5
	21450535.MAK	7.1	15.60+0.15	15.67+0.05	+0.41/15.64	5.8
	21450534.ESDC	66.8	14.95+0.22	15.02+0.09	+1.62/14.97	5.4
Earthquakes	21456615.WMQ	0.4	13.92+0.14	14.01+0.05	+3.64/13.93	3.2
	21456712.ARU	22.2	14.44+0.25	14.44+0.24	-8.70/14.48	3.8
	21457058.ILAR	65.3	15.55+0.27	15.45+0.10	-11.18/15.59	4.3

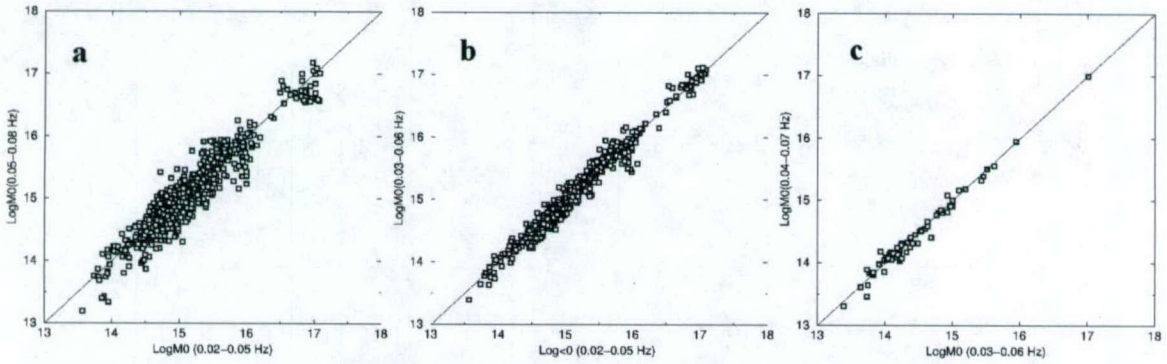

Figure 22. Comparison of station spectral magnitudes in different frequency bands: (a) adjacent bands, all distances; (b) overlapping bands, all distances; (c) overlapping bands, distances $\leq 5^{\circ}$.

Next, we examined the consistency of spectral magnitude estimates in different frequency bands. Figure 22 shows examples of such estimates in several frequency bands (marked along the plot axes). These results indicate that although measurements are generally consistent when measured in different frequency bands, some individual measurements do change significantly. Also, there is a tendency for measurements to be smaller at higher frequencies (points lie slightly to the right of the lines in Figure 22). These results indicate that spectral magnitudes can be measured in different frequency bands, but with some caution and attention to spectral shape variations.

We examined which frequency bands performed best for discrimination between small earthquakes and explosions. That is, we evaluated whether any set of variable frequencies discriminate better than a single frequency band applied at all distances. Figure 23 (left) shows logM_0:m_b plots using a set of variable frequencies (0.02-0.05 Hz for distances exceeding 25°, 0.06-0.09 Hz for 10° to 25°, and 0.08-0.11 Hz for distances below 10°). In a large statistical analysis of measurements made in different frequency bands at different distances, these frequency bands were found to be the optimum for measurement, based on best signal to noise and flat spectral shape. Figure 23 (right) shows logM_0:m_b plots using the 0.03-0.07 Hz frequency band for all distances.

The plot on the left, where higher frequencies are used at small distances (and hence for the smallest earthquakes) appears to discriminate less well for small events than when a constant 0.03-0.07 Hz frequency band is used for the magnitude measurements. We examined the logM_0:m_b ratio for a number of frequency bands and established that the 0.03-0.07 Hz interval performs best for discriminating between earthquakes and explosions for the Lop Nor data set. This effect might be expected from the path corrected spectra shown in Figure 16, since the earthquake spectra exhibit a slow decline in amplitude with frequency. This experiment demonstrates a potentially important tradeoff – for small events higher frequencies may provide the best signal to noise performance, but have degraded discrimination capability.

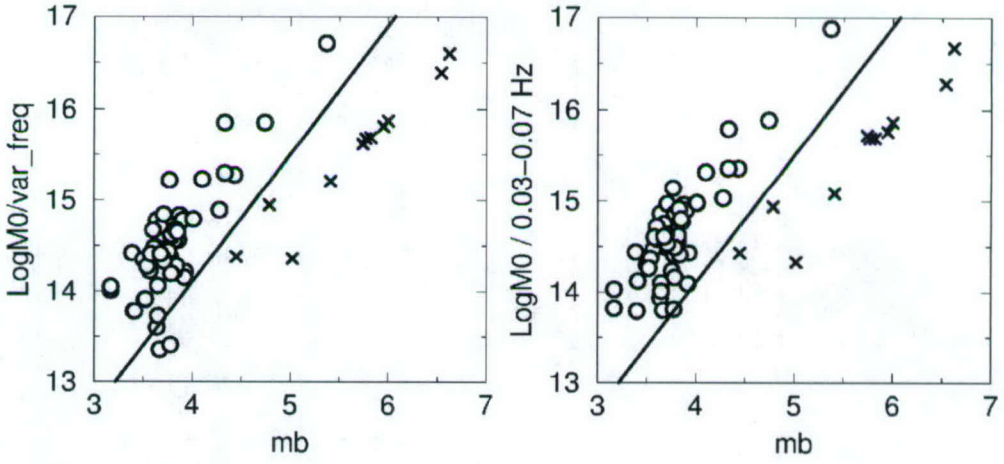

Figure 23. LogM_0:m_b plots showing event spectral magnitudes for earthquakes (O) and explosions (X) in Lop Nor. Station spectral magnitudes were calculated using frequencies increasing with decreasing distance (left) and the 0.03-0.07 Hz frequency band for all distances (right). Bold lines mark the empirical discrimination relationship of Stevens and McLaughlin (2001). For small events higher frequencies may provide the best signal to noise performance, but at a cost of degraded discrimination capability.

4.3 Path Corrected Noise Estimates at the Lop Nor Test Site

While a path corrected spectral magnitude can be measured over any frequency band, it is subject to the following constraints:

1. Earthquake spectra decrease at high frequencies, depending on depth (see Figure 16), so the high end of the frequency band should be low enough that discrimination is not degraded by this effect.

2. At high frequencies, attenuation is greater and the dispersion more variable, so the path correction is likely to be less well determined and the signal may be smaller than at lower frequencies, particularly at longer distances.

3. Noise increases at low frequency, so the low end of the frequency band should be high enough to be above the noise level.

In order to quantify these effects, we created some "path corrected noise spectra" using path corrections appropriate for the Lop Nor test site. These are simply noise spectra measured at the station that have been divided by an explosion Green's function in the same manner as would be done for a signal. Since the signal spectra are approximately flat over most of the frequency band, the path corrected noise spectra are a measure of the minimum path corrected signal that could be measured at each station.

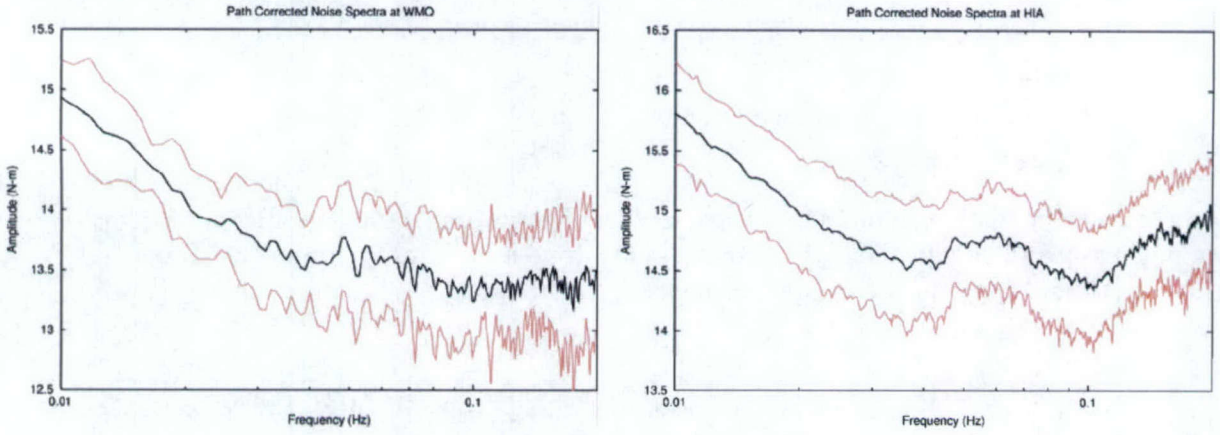

Figure 24. Average "path corrected noise measurement" and ±one standard deviation curves for 13 time segments at WMQ (left) and for 54 time segments at HIA (right). The path corrected noise measurement gives the minimum path corrected signal level that could be observed at each frequency. Recall that the predicted path corrected explosion spectrum is flat over this frequency band, and the predicted path corrected earthquake spectra *decrease* with increasing frequency (see Figure 16).

Figure 24 shows the path corrected noise measurements for two stations: WMQ, located an average of 2 degrees from each event, and HIA, located an average of 27 degrees from each event. At HIA, the noise spectrum has minima at 0.04 and 0.1 Hz, either side of the 0.06 Hz primary microseism peak. Noise amplitudes increase substantially below about 0.04 Hz. Noise levels at WMQ are similar, but are flatter from 0.04 to 0.2 Hz with a less prominent microseism peak and lower (path corrected) noise at the highest frequencies because of the close distance. As Figure 24 shows, there is also considerable variability in the noise level, so that although the average noise level is about 13.5 at WMQ and 14.5 at HIA (corresponding approximately to M_s

1.7 and 2.7, respectively), the minimum spectral magnitude that could be measured may be substantially lower or higher depending on the noise level at the time the measurement is made.

These results suggest that in general it is best to measure surface wave spectra at frequencies above 0.03 Hz and below 0.1 Hz. Although noise levels remain fairly low in the 0.1-0.2 Hz frequency band at the closest stations, factors #1 and #2 mentioned above make measurement in this band risky. Based on a number of empirical tests, we recommend measuring surface waves at frequencies between 0.03 and 0.08 Hz for this region. Further research is required to determine the optimum frequency band in other regions where there are structures that cause large amplitude changes, such as along paths that cross oceanic regions.

4.4 Comparison of Spectral and Time Domain Magnitudes

Russell (2004) proposed a new type of surface wave magnitude $M_{s(b)}$ which differs from a traditional 20 second magnitude in that it uses a Butterworth filter to measure a time domain amplitude in a narrow band around any desired frequency, and then applies a correction for the source function similar to the explosion source function used in the path corrected spectral magnitude described above. The main purpose of $M_{s(b)}$ is to allow surface waves to be measured at regional distances at higher frequencies. The magnitude is defined by:

$$M_{s(b)} = \log(A_b) + \frac{1}{2}\log(\sin\Delta) + 0.0031\left(\frac{20}{T}\right)^{2.3}\Delta - 0.66\log\left(\frac{20}{T}\right) - \log(f_c) - 0.43 \qquad (4.2)$$

where A_b is the filtered amplitude, T is the measured period, and f_c is the Butterworth filter width. It is instructive to compare the terms in the Russell magnitude with the Rezapour and Pearce (1998) M_s and the path corrected spectral magnitude $\log M_0$ described above. This is shown in Table 2.

Table 2. Comparison of time domain and spectral magnitude measurement and correction terms.

Magnitude Type	Amplitude Measure	Source	Receiver	Geometric Spreading	Attenuation	Dispersion	Filter	Norm
M_s	log(A/T)			$\frac{1}{2}\log(\sin\Delta)$	0.0046Δ	$\frac{1}{3}\log\Delta$		2.37
$M_{s(b)}$	$\log(A_b)$	$-0.66\log\left(\frac{20}{T}\right)$		$\frac{1}{2}\log(\sin\Delta)$	$.0031\left(\frac{20}{T}\right)^{2.3}\Delta$		$-\log(f_c)$	-0.43
$\log M_0$	$\log(A_s)$	$-\log(S_1)$	$-\log(S_2)$	$\frac{1}{2}\log(\sin\Delta)$	$\gamma_p\Delta$			

Note that each magnitude makes a slightly different set of corrections. $\log M_0$ corrects for both source and receiver structure based on earth models at those locations and using an explosion Green's function at the source. Similarly, $M_{s(b)}$ applies a source correction based on typical explosion source excitation. The Airy phase dispersion correction accounts for superposition of waves with similar group velocities, and is needed only in the time domain. $M_{s(b)}$ uses a Butterworth filter that is sufficiently narrow to avoid this problem. The filter correction corrects

for the width of the Butterworth filter. The normalization for the two M_s measurements is chosen to make it consistent with historical M_s magnitudes at a chosen distance range. $\log M_0$ has natural units of log moment and is not otherwise normalized, however Stevens and McLaughlin (2001) showed that $\log M_0 - 11.75$ is consistent with the Rezapour and Pearce M_s. Attenuation for M_s is an empirical correction based on a very large number of 20 second measurements. $M_{s(b)}$ similarly uses an empirical attenuation correction, but also includes an empirical correction for the change in attenuation with frequency. $\log M_0$ uses attenuation calculated from earth (velocity, density and Q) models along a source to receiver path.

A path corrected time domain magnitude can be derived by combining the path corrected spectral magnitude with $M_{s(b)}$, using the source and path corrections from earth models to replace the empirical average corrections. We define the path corrected time domain magnitude $M_{s(bp)}$ as:

$$M_{s(bp)} = \log(A_b) + \frac{1}{2}\log(\sin\Delta) + \gamma_p \Delta - \log(S_1) - \log(S_2) - \log(f_c) + C_{bp} \qquad (4.3)$$

where C_{bp} is a constant chosen to make $M_{s(bp)}$ consistent with historical magnitudes. Although equation 4.3 may appear more complicated than equation 4.2, the functions S_1, S_2, and γ_p are easily tabulated and stored in files, and a computer can quickly calculate them for any path based on a simple lookup table. There is substantial regional variation in these quantities that should be removed to ensure consistent measurements (examples of S_1, S_2, and γ for continental and oceanic structures are shown in Stevens and McLaughlin, 1996). Another advantage of this approach is that it can ensure that f_c, which must be less than a minimum value calculated from the group velocity, is always set appropriately.

Bonner et al. (2004) showed that $M_{s(b)}$ gave consistent results as a function of distance, and also gave good discrimination results when the maximum value of $M_{s(b)}$ over the entire frequency band was used. This result could be expected from Figure 16, showing the frequency variation of earthquake spectra as a function of depth, and from Figure 19, showing the variability of measured path corrected earthquake spectra. By taking the maximum value of $M_{s(b)}$ instead of measuring all surface waves at the same frequency, $M_{s(b)}$ can move to lower frequencies for earthquakes, avoiding the spectral reduction at higher frequencies, and can avoid spectral dips that commonly occur in real data. This may, therefore, be a better approach to measuring surface waves for discrimination than the distance dependent or fixed frequency band spectral methods described above. However, some caution is necessary since as shown in Figure 24, noise increases rapidly at lower frequencies, so the maximum value could easily correspond to a noise measurement even when a surface wave is clearly visible at higher frequencies.

5 BACKAZIMUTH ESTIMATION RELIABILITY USING SURFACE WAVE POLARIZATION

As part of its responsibilities under the Comprehensive Nuclear-Test-Ban Treaty (CTBT), the International Data Center (IDC) automatically processes seismic data recorded at International Monitoring System (IMS) stations, identifying surface waves and measuring surface wave amplitude and M_s (Stevens and McLaughlin, 2001). The M_s measurement is important because of the earthquake/explosion discrimination capability of the M_s:m_b discriminant (e.g. Marshall and Basham, 1972; Stevens and Day, 1985). Three-component backazimuth estimates derived using the current, spectral method are recorded but are too inaccurate to use for association. That method is based on an algorithm originally proposed (Smart, 1978) as part of a surface wave detector, rather than as a means of estimating the backazimuth. Selby (2001) suggested that another detection technique (Chael, 1997), based on cross-correlation of the vertical and Hilbert transformed radial component Rayleigh wave records, could be used for backazimuth estimation and would improve IDC processing.

To compare the performance of the algorithms, we incorporated the Chael/Selby (CS) algorithm into the automatic surface wave processing software that utilizes the current IDC method (CM). Under current IDC procedures, for an event location and time based on body wave arrivals, a surface wave is considered detected if it passes a dispersion test in the group velocity window predicted for the event. We test both algorithms on 2,599 records that passed the dispersion test and 2,363 generally poorer S/N records that failed, all from events that had at least four surface wave detections. We assess the performance of each algorithm for different passbands and group velocity windows.

5.1 Differences Between the Azimuth Estimation Algorithms

Both the CM and CS algorithms find the backazimuth that best matches the expectation that the horizontal and vertical components of the Rayleigh wave records are similar, but 90° out of phase. The biggest difference between algorithms is that CM uses Love as well as Rayleigh waves to estimate the backazimuth. Consequently, the CS algorithm should perform optimally when the time window encompasses just the Rayleigh wave, as a longer window will only add noise, while the CM should perform optimally with a longer time window that encompasses both the Rayleigh wave and the higher group velocity Love wave.

5.1.1 The Current Method

The CM finds values for r_n and l_n, the complex Fourier coefficients of the Rayleigh and Love wave vertical component displacements, ϕ, the backazimuth, and ε_n, the Rayleigh wave ellipticity, that minimize the squared distance between the data and model (Smart, 1978; Smart and Sproules, 1981). The ellipticity may be assumed known, which reduces by one the degrees of freedom. Subscripts refer to frequency. The function minimized is

$$\sum_n \left|z_n - r_n\right|^2 + \left|y_n - \left(i\varepsilon_n r_n \alpha - l_n \beta\right)\right|^2 + \left|x_n - \left(i\varepsilon_n r_n \beta + l_n \alpha\right)\right|^2 \qquad (5.1)$$

where x_n, y_n, and z_n are the complex Fourier coefficients of the east, north, and vertical components of the seismic record at the n^{th} frequency, and α and β are $\cos(\phi)$ and $\sin(\phi)$ respectively. Two important elements of this function are that the radial component of the Rayleigh wave equals $i\varepsilon_n r_n$, that is, the vertical component advanced by 90° and scaled by the ellipticity, and that the Love wave is independent of the Rayleigh wave.

5.1.2 The Chael/Selby Algorithm and its Implementation

The CS algorithm (Chael, 1997; Selby, 2001) finds the backazimuth for which the correlation coefficient of the vertical and Hilbert transformed radial is a maximum (Equation 5.2).

$$C_{z\bar{r}} = \frac{S_{z\bar{r}}}{\sqrt{S_{zz} S_{\bar{r}\bar{r}}}}, \tag{5.2}$$

where,

$$S_{jk} = \sum_{\tau=1}^{N} x_j(\tau) x_k(\tau). \tag{5.3}$$

The implementation uses the cross-correlation of the Hilbert transformed vertical with the radial, for one degree increments of backazimuth. While Selby uses the maximum positive cross-correlation as the backazimuth, Chael (1997) uses the central azimuth, determined by the circular mean (e.g. Fisher, 1993). We test the algorithm using both measures.

For synthetic Rayleigh waves with azimuthally evenly distributed random noise, the circular mean provides more accurate estimates than the maximum cross-correlation. The lower the S/N, the greater the advantage of the circular mean.

For noise free data (i.e. synthetics), equation 5.2 will return a negative or positive constant, as the numerator changes in synch with the second term of the denominator (the first denominator term is constant) as the algorithm steps through backazimuth. Our implementation of the algorithm therefore provides two methods of estimating the similarity of the components. One uses the correlation coefficient (equation 5.2). The second method is intended to avoid the problem described above when data are noise free by normalizing by S_{zz} alone (equation 5.4).

$$C_{z\bar{r}} = \frac{S_{z\bar{r}}}{S_{zz}}. \tag{5.4}$$

5.2 Performance of the Algorithms in 4 Frequency Bands

The first set of tests used a 2.5 to 5.0 km/sec group velocity window, which should encompass both Love and Rayleigh waves, and compared backazimuth estimates in 3 relatively narrow, overlapping frequency bands, 0.02-0.04 Hz, 0.03-0.05, 0.04-0.06 Hz, plus one frequency band covering the entire spectrum from 0.02 to 0.06 Hz.

Figure 25 shows histograms of backazimuth residuals for the CM and one implementation of the CS algorithm for the middle frequency band. Table 3 presents the errors associated with each

method. The CS algorithm performs better in two ways. First, the CM applied as it is currently used in the automatic processing, has errors of 180° for a significant number of events. Second, the histograms reveal many more outliers for the CM than for the CS algorithm.

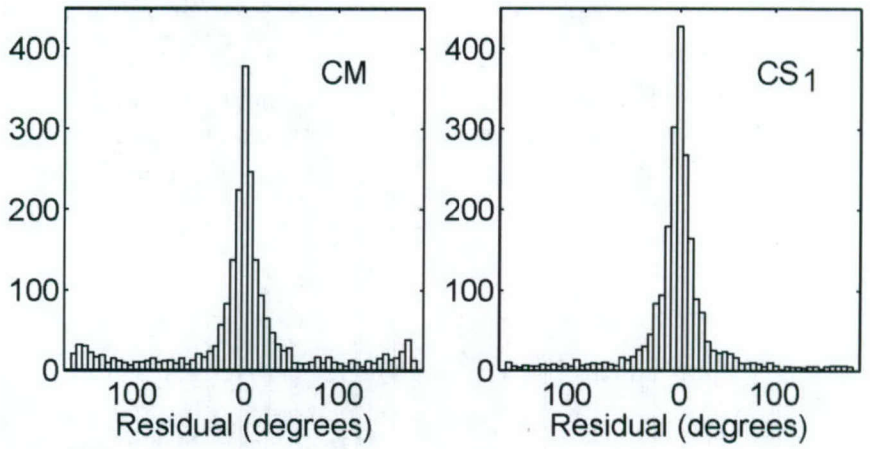

Figure 25. Backazimuth residuals for 0.03-0.05 Hz using the current method (left) and the Chael/ Selby algorithm using the normalization of equation 5.2 and peak cross-correlation (right).

Surprisingly, the best implementation of the CS algorithm is the combination of the peak position of the cross-correlation and normalization of the correlation by $\sqrt{S_{zz}S_{\overline{rr}}}$. Why the maximum cross-correlation provides a more accurate estimate of backazimuth than the circular mean bears further investigation. One possibility is that the real noise is azimuthally unevenly distributed, consistent with observations of Selby (2001), and so biases the circular mean measurement toward the direction of the predominant noise source. Such skewed noise would not so strongly affect the maximum cross-correlation position.

We use the scaled median absolute deviation (SMAD), the one-norm measure of the central tendency, to provide a measure of the spread of data about the central value that is less biased by outliers than the STD in heavy-tailed data such as these.

The CM performs best at higher frequency, while the CS algorithm performs best at lower frequency. The CM performs almost as well as the CS algorithm at the highest frequencies tested. This is likely because the Love waves are relatively larger at longer periods than the Rayleigh waves, and contrary to expectations, the CM performs poorly when the Love waves are very large. This is due to the 180 degree ambiguity in Love wave polarization, which causes large Love wave amplitudes to increase the likelihood of a 180 degree error in backazimuth. Larger backazimuth residuals at higher frequency for the CS method are due to lower S/N.

For the CS algorithm, the backazimuth residuals for the broader frequency band are comparable to those in the 0.03-0.05 Hz passband, larger than those of the lowest frequency passband, and smaller than those of the highest frequency passband. The parts of the frequency band where the backazimuth either varies or is less well resolved diminish resolution of the broadband estimate

compared to narrower passband estimates, so the broader frequency band does not provide an advantage. For the CM, the performance is poorer for the broadband data than for each of the narrower passbands used. The rest of the analyses are performed for just the three narrow frequency bands.

Table 3. Scaled median absolute deviations and standard deviations (in parentheses) of the backazimuth residuals in 4 frequency bands from the algorithms tested. Four variations of the implementation of the CS algorithm are tested. CS_1 and CS_2 use the peak amplitude of the cross-correlation while CS_3 and CS_4 use the circular mean. CS_1 and CS_3 are normalized by $\sqrt{S_{zz}S_{\overline{rr}}}$ as in equation 5.2. CS_2 and CS_4 are normalized by S_{zz} as in equation 5.4.

	.02-.04 Hz	.03-.05 Hz	.04-.06 Hz	.02-.06 Hz
CM	31 (85)	22 (71)	22 (64)	20 (68)
CS_1	13 (41)	16 (47)	19 (53)	16 (45)
CS_2	17 (40)	19 (46)	22 (52)	20 (45)
CS_3	15 (39)	17 (46)	20 (52)	17 (45)
CS_4	17 (40)	19 (46)	22 (53)	20 (45)

5.3. The Effect of Signal Strength (Event Size) on Backazimuth Estimates

Figure 26 shows the backazimuth residuals for each of the algorithms vs. event size, which serves as a proxy for the signal-to-noise ratio. For large events, the CM's performance is almost comparable to the CS algorithm's, except for a large number of sign errors. The greatest advantage of the CS algorithm is in estimating backazimuth of smaller events, especially at lower frequency, where the CM fails badly.

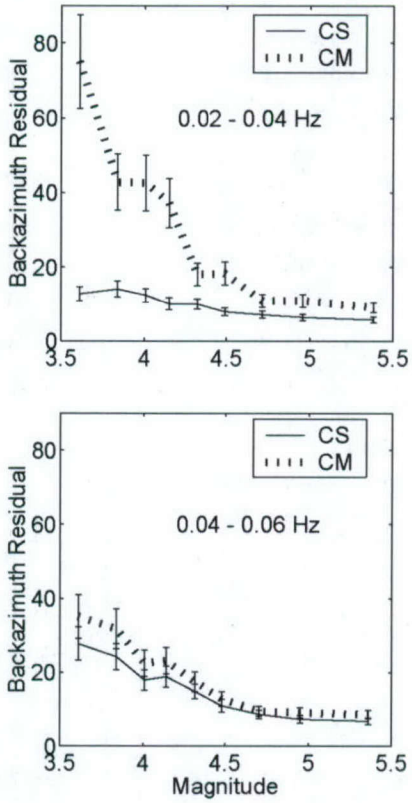

Figure 26. Median ±2 SMAD confidence intervals of backazimuth residuals binned by M_s values for the CM (dotted) and CS_1 algorithm (solid). Each bin has 250 backazimuth residuals. Results at 0.03-0.05 Hz are intermediate between those shown.

5.4 The Effect of Variable Group Velocity Windows

The work reported above used 2.5 to 5.0 km/sec group velocity windows that we expected to favor the CM, as they are most likely to include both Love and Rayleigh waves. Next we use the group velocities predicted by a 1° global surface wave model (Stevens, et al 2001) to select windows intended to more narrowly bracket the Rayleigh waves and so minimize the effect of noise outside those windows (Figure 27). The minimum group velocity is that used in the dispersion test for surface waves at the high frequency limit of the passband. Similarly, the maximum group velocity is determined by the low frequency limit.

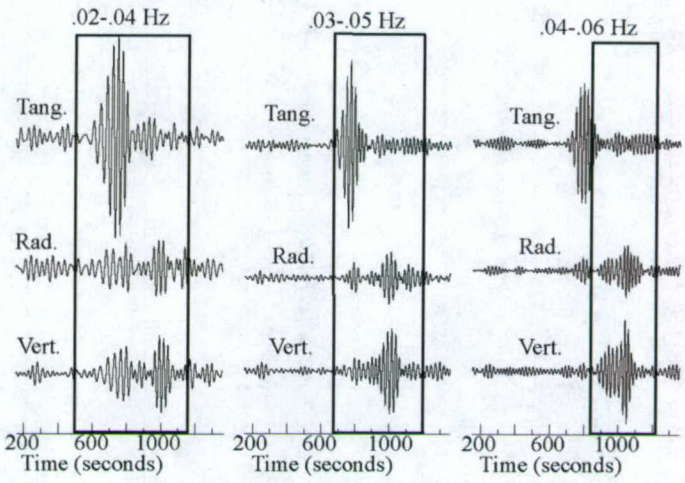

Figure 27. Surface waves in the 3 passbands tested, at the station ARCES, for an Ms 5.0 event at 6035 km. The entire trace is the 5.0 to 2.5 km/s group velocity window. Outlined segments are the shorter group velocity windows used to isolate the Rayleigh waves. The isolation works best in the highest frequency band, where the large Love wave (top trace) is outside the narrower window.

Table 4 is similar to Table 3, but for the variable length group velocity windows. The performance of the CM is slightly worse for the shorter windows at the highest frequency passband, as expected, and there is a small improvement in performance of CS_1 compared to the longer group velocity windows. Overall, the effect of narrowly isolating the Rayleigh waves is small, which is encouraging for future implementation of the CS algorithm for routine detection.

Table 4. Same as Table 3, but for group velocity windows designed to isolate the Rayleigh waves. The change from the 2.5 to 5 km/s group velocity windows is given in parentheses (negative change is improvement).

	.02-.04 Hz	.03-.05 Hz	.04-.06 Hz
CM	31.4 (+0.7)	21.2 (-0.4)	23.9 (+1.5)
CS_1	12.7 (-0.5)	14.9 (-0.8)	18.1 (-0.5)
CS_2	17.0 (+0.5)	19.0 (+0.3)	21.5 (-0.3)
CS_3	14.7 (-0.1)	16.8 (-0.2)	19.6 (-0.4)
CS_4	16.9 (+0.4)	19.0 (+0.2)	21.6 (-0.2)

5.5 Predicting Accuracy of Estimates Using the Cross-Correlation Value

The value of the cross-correlation of the Hilbert transformed vertical with the radial, $C_{\bar{z}r}$, predicts the accuracy of the backazimuth estimate. Figure 28 (right) shows backazimuth residuals vs. $C_{\bar{z}r}$ for CS_1, applied to data that pass the dispersion test. The plot shows the median ± two SMAD confidence intervals for bins with 171 azimuth residuals each versus the median $C_{\bar{z}r}$ value for each bin. The histograms show azimuth residuals for all the data that pass the dispersion test (left), and just those with $C_{\bar{z}r} \geq 0.8$ (right).

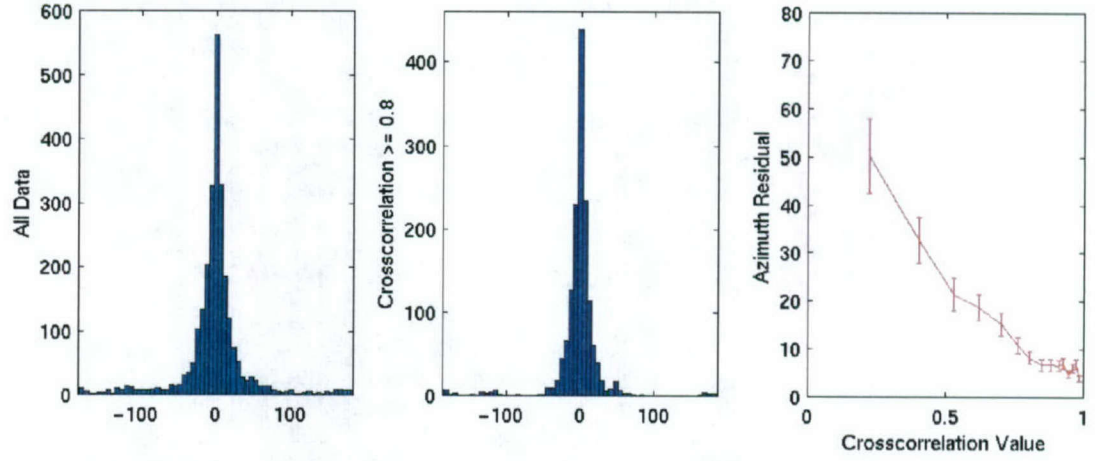

Figure 28. Median azimuth residuals ±2 SMAD confidence intervals vs. the correlation of the radial and Hilbert transformed vertical Rayleigh waves for the 0.03-0.05 Hz passband. Results are similar for the other passbands.

At 0.02 to 0.04 Hz, the cross-correlations ($C_{\bar{z}r}$) of 60% of the data are ≥ 0.8. The SMAD of the backazimuth residuals of those data is 8.5°, vs. 25.2° for data with $C_{\bar{z}r} < 0.8$. At 0.03 to 0.05 Hz, the 58% of the data that have $C_{\bar{z}r} \geq 0.8$ have a SMAD of 9.3° vs 28.8° for the data with $C_{\bar{z}r} < 0.8$. At 0.04 to 0.06 Hz, the 54% of the data that have $C_{\bar{z}r} \geq 0.8$ have a SMAD of 11.1° vs 35.8° for the data with $C_{\bar{z}r} < 0.8$.

This ability to predict backazimuth estimate accuracy can aid association with known events. In particular, the strict dispersion criteria for detection at the IDC could be relaxed in cases where the backazimuth is consistent with the theoretical backazimuth and the cross-correlation value is high.

5.6 Performance on Events for Which Surface Waves Are Not Detected

Figure 29 shows the results of each method of polarization analysis applied to the poorer S/N records that did not pass the dispersion test. The CS1 implementation extracts accurate backazimuth estimates for very many of these data. The more accurate estimates can be identified by their cross-correlation value.

The SMAD of the CS backazimuth residuals for all data not passing the dispersion test is 58°, vs. 108° for the CM. The middle plot shows histograms just for data with a cross-correlation ≥ 0.8, which comprise 14.7% of the data. Their backazimuth residual has a SMAD of 14.8°. The F-statistic of the CM does not provide similar predictive capabilities. In fact, for the largest F-statistic values, the CM's error increases. This is because the F-statistic can be very large when the signal is dominated by very large Love waves, but such records often have 180° (i.e. sign) errors. Even disregarding the sign errors, the F-statistic is a much poorer predictor of the accuracy of polarization estimates, and the resolution of the CM is much poorer than that of the CS algorithm.

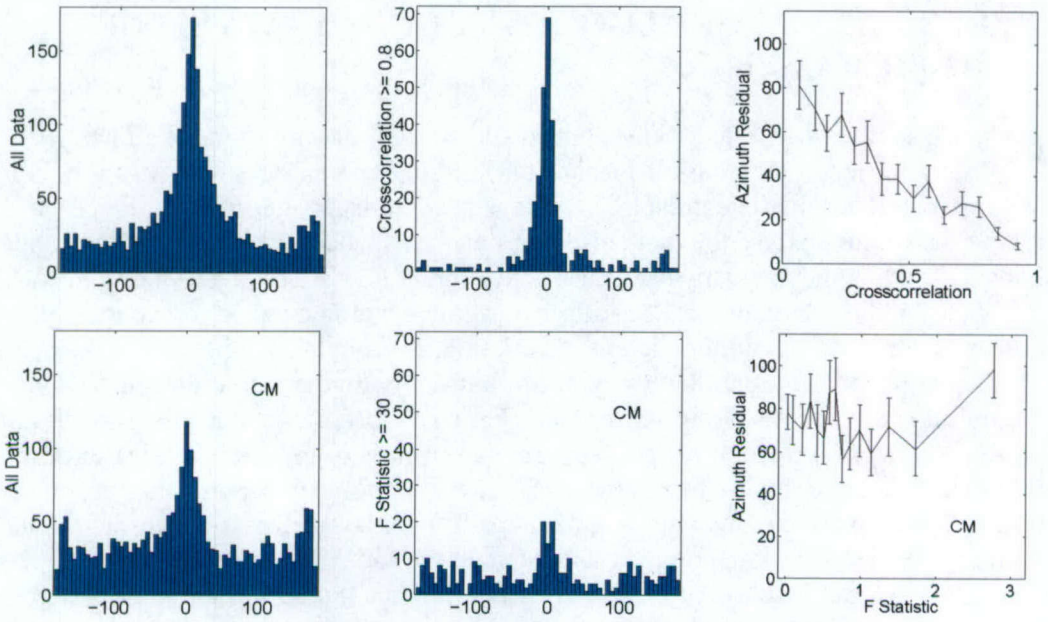

Figure 29. Azimuth residuals for the 0.02 – 0.04 Hz passband for the CS algorithm (top row) and the CM (bottom row). Histograms of azimuth residuals for all the data (left column) and for data with correlation ≥ 0.8 for CS (upper middle) or F-statistic ≥ 30 for the CM (lower middle). The middle plots use ~14.5% of the data in each case. The upper right plot shows the median azimuth residual ±2 SMAD confidence intervals vs. the correlation, as in Figure 28, for the CS algorithm. The bottom right shows the median azimuth residual ±2 SMAD confidence vs. the F statistic of the CM.

6 PERFORMANCE OF ALGORITHMS AND ANALYSIS OF "PROBLEM CASES"

In many respects surface waves are well-behaved and straightforward to model. Two characteristics in particular are helpful: 1) since the surface wave always follows a minimum time path, any path other than the great circle path is necessarily longer, which reduces the error in the travel time (in inversions, the main effect of this is to make low velocity regions appear somewhat smaller than they actually are (e.g. Ritzwoller, et al, 2002)); and 2) along most continental paths at the regional distances of greatest interest today, and at the periods greater than 10 seconds which are recommended for discrimination, amplitude differences due to variations in attenuation are small. Only regions of unusually high attenuation cause significant errors in amplitude predictions along short paths. For most surface wave studies, uncertainties in event location and measurement error are responsible for more of the unmodelable error than actual differences due to complexities in the earth. There are some exceptions to this, however. In cases where surface waves travel along grazing paths near large changes in earth structure, surface waves can be much more complex and difficult to model. Multiple interfering or distinct surface wave arrivals can be observed that take different paths through or around a low velocity region (Figure 30). The Tarim Basin in western China is a particularly strong example of this effect. In this case, dispersion models can at best predict the dominant surface wave arrival, and the amplitude may not be predictable without detailed analysis of the data and the earth structure that causes the variations. One technique that we found to help for achieving consistency of measurement and reliability of the inversion is to review the data and order (select) the arrivals such that the dispersion picks change from fast to slow to fast smoothly as the azimuth changes across the basin. Although this doesn't completely resolve the multiple arrival problem, it selects the arrivals in a manner consistent with waves traveling on a continuous set of paths across the complex earth structure. This still does not lead to a satisfactory solution for grazing paths at higher frequencies, however, as illustrated in Figures 31 and 32.

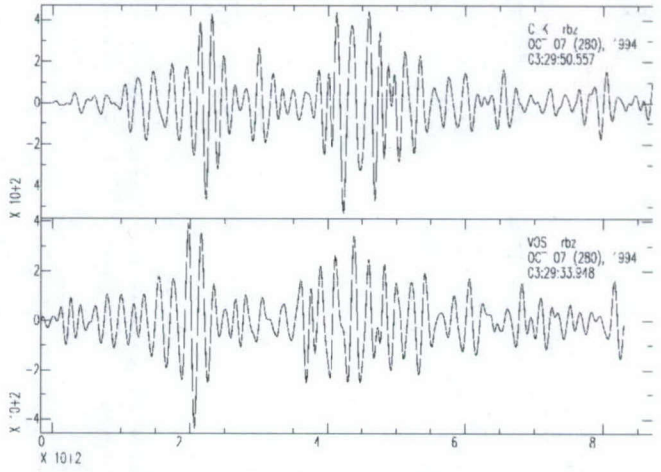

Figure 30. Seismograms recorded at two stations on paths passing through the Tarim Basin. There are two distinct surface wave arrivals of comparable amplitude. The second arrival is dominant for paths traveling directly through the basin, and the first arrival is dominant for paths near the basin boundary.

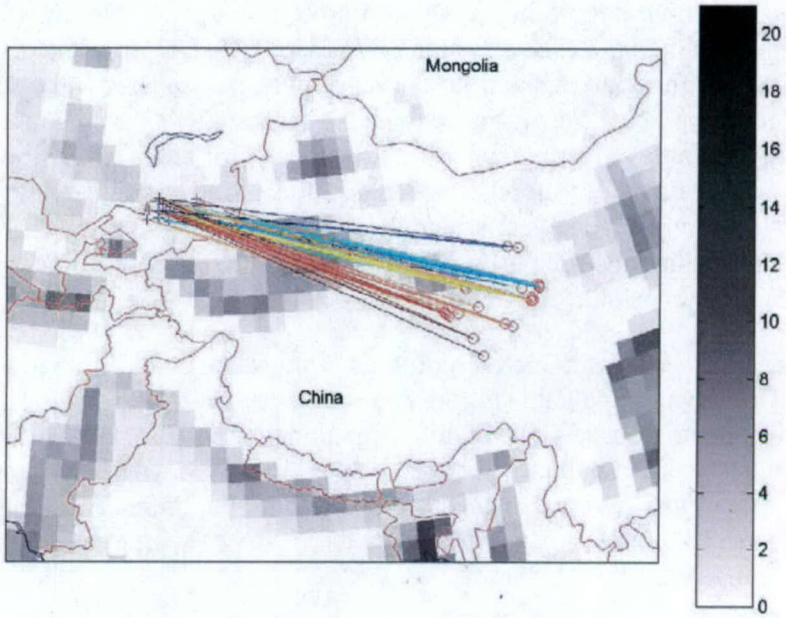

Figure 31. Paths near and across the Tarim Basin. Colors correspond to the colors on the dispersion curves in Figure 32.

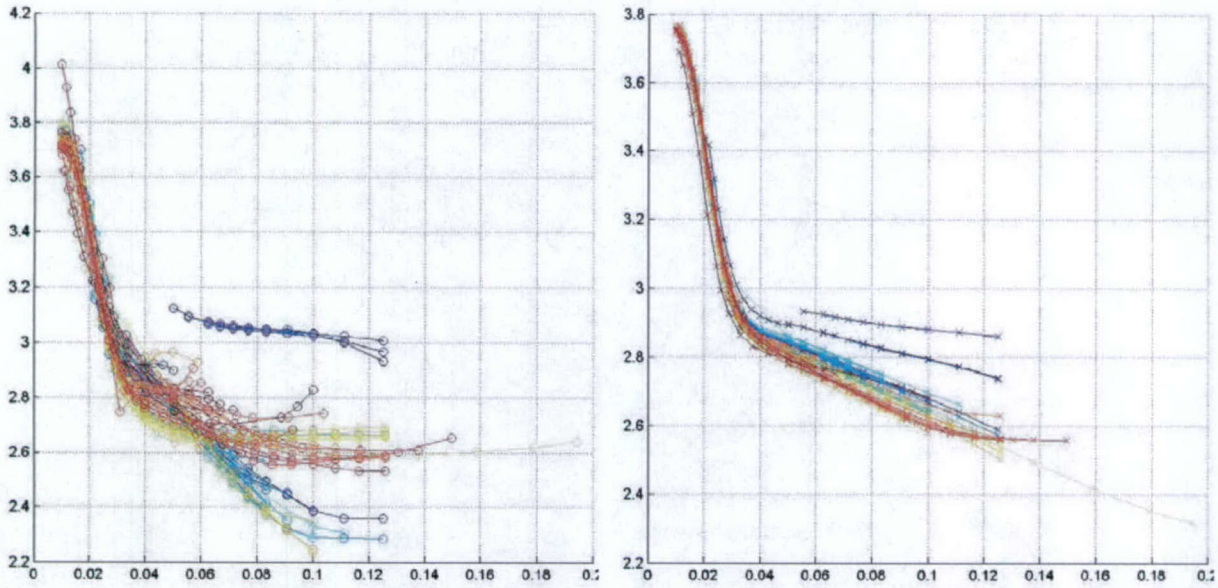

Figure 32. Observed (left) and calculated (right) dispersion curves for the paths shown in Figure 31. Colors correspond to the paths on the map in Figure 31.

To determine the dispersion curve for a particular path, we use the narrow-band filtering algorithm originally due to Dziewonski et al. (1969) as implemented by Stevens and McLaughlin (2001). This method applies ~50 narrow Gaussian filters to a vertical seismogram, calculates the envelope function, and then determines the time and instantaneous frequency of each peak. The

peaks are due not only to the Rayleigh wave of interest, but also to other interfering phases, higher modes, multi-pathed arrivals, and noise. We identify the appropriate dispersion curve by connecting the most significant peaks from the set of peak frequencies and times, which have been converted to group velocities. It begins with the largest peak, and then moves out in both directions finding the largest nearby peak. This works well for cases where the Rayleigh wave is separated in frequency or time from other arrivals, which is the case for many records, but will not work well over frequency bands in which there are interfering arrivals closely spaced in both time and frequency. Situations such as the Tarim Basin can create multiple interfering surface waves in some frequency bands.

Figure 33 shows 2 sets of 3-component recordings of the same event, filtered from 10 to 20 second period. The propagation path (Figure 34) for the record on the left is uncomplicated, and the records show a distinct Love wave on the tangential component, and a distinct Rayleigh wave on the radial and vertical components. It appears that the surface waves come in somewhat off azimuth, as there is a little Love wave energy on the radial, but there is none clearly on the vertical and the corresponding selection of a dispersion curve is straightforward and matches the model well (Figure 35).

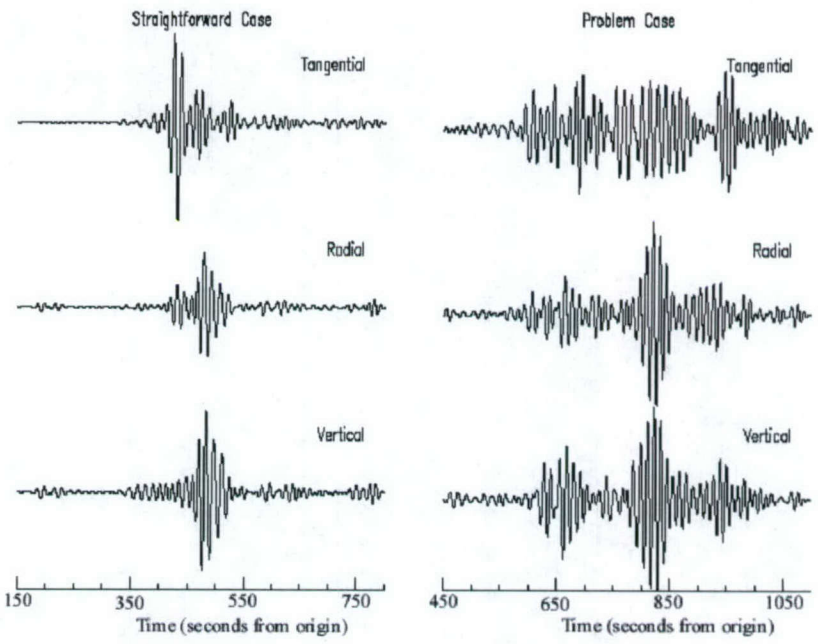

Figure 33. 3-component surface waves for recordings of a single event with one path crossing (right) and one not crossing (left), the Tarim Basin. Source-station distances are 1,427 km (left) and 1,918 km (right).

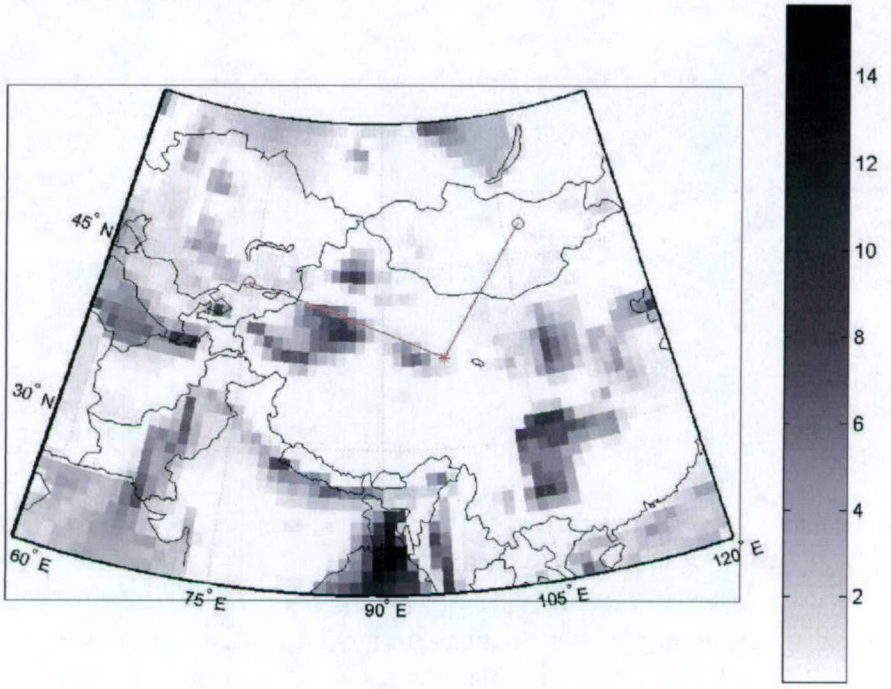

Figure 34. Propagation paths overlain on a sediment thickness map (contoured in kilometers by grayscale darkness) for the uncomplicated records on the left side of Figure 33 (propagating to the northeast) and the complicated records, which propagate west through the thick sediments of the Tarim Basin.

The propagation path (Figure 34) of the record on the right of Figure 33 traverses the Tarim Basin and appears to have two Rayleigh waves that interfere in the frequency band from 0.04-0.06 Hz and become distinct at higher frequencies. In this case, the automatic pick of the dispersion curve jumps from higher to lower velocity between .045 and .055 Hz, as it jumps from the more coherent lower frequency Rayleigh wave to the later (and larger) of the two higher frequency Rayleigh waves (Figure 35).

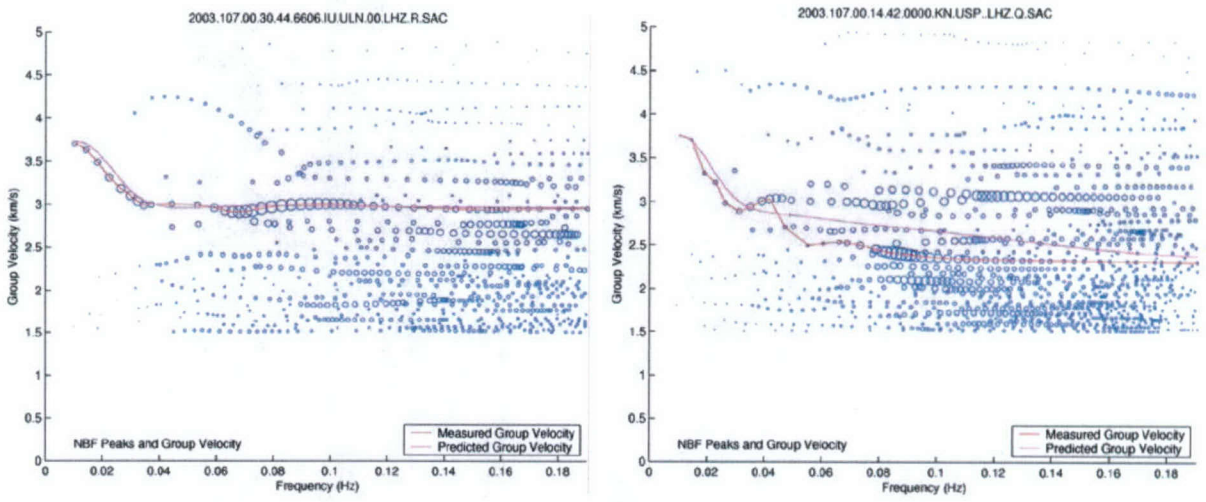

Figure 35. Dispersion curves (red) picked for the vertical component records shown in Figure 33, compared with the model based prediction (maroon).

In this application, we are trying to measure dispersion curves to use in tomographic inversion for earth structure. How do we use data such as that shown in the right hand side of Figure 35? We could simply throw out the data as unreliable, but then would lose constraints on earth structure in a complicated area. We could decide to always take the fastest arrival, which generally tends to be more consistent, but that biases the data set in favor of arrivals that travel on faster paths, such as around the Tarim Basin rather than through it. The most disastrous approach is to inconsistently choose the faster or slower branches for nearby paths, in which case no consistent earth model is possible. The best approach appears to be to use the Rayleigh wave that travels closest to a great circle path, and to not use frequency bands where there is strong interference. Following is one method for accomplishing this.

To consistently identify the "same" Rayleigh wave from successive events, i.e. one that takes a similar path, we first identify the reason for there being two (or more) separate Rayleigh waves in seismograms with paths crossing the Tarim Basin. One hypothesis is that the later arrival has taken the more direct, but slower path through the basin, while the earlier arrival has taken a separate path around the basin. A second possibility is that the earlier Rayleigh wave is a converted Love wave. That is, the strong lateral velocity contrast at the basin could rotate the Love wave so that it is partly polarized to the vertical. Similar observations, termed quasi-Love waves, were made for paths to Hawaii (Levin and Park, 1998), in that case attributed to lateral changes in anisotropy.

The polarization algorithm presented in the previous section provides a means of identifying the Rayleigh wave path. The correlation of the Hilbert transformed radial with the vertical record provides a means of identifying Rayleigh waves and estimating their polarization direction. Figure 36 (top row) shows the vertical seismogram of the problem case of Figure 33, filtered from 10-20 seconds period (left) and 5-10 seconds period (right). In the lower frequency case, the later Rayleigh wave is larger. The backazimuth providing the maximum correlation of the Hilbert transformed radial with the vertical component is found for a moving window 3 times the center period of the passband. The overlap between windows can be as small as necessary for

refining pick times. The maximum correlation of each window (second row) identifies both Rayleigh waves, with the second being dominant. The third row shows the backazimuth vs. time. For the lower frequency, the backazimuth of the second Rayleigh wave, at ~820 seconds (2.34 km/s) is 88°, 13° off azimuth to the north of the theoretical backazimuth of 101°. The backazimuth of the earlier arrival, at 650 seconds (2.95 km/s) is 67°, 34° off azimuth to the north. This is consistent with the earlier Rayleigh wave traveling around the Tarim Basin to the north, while the second one travels through the basin, albeit possibly also traveling through the shallower part of the basin somewhat to the north of the great circle path.

The higher frequency records (Figure 36, right) require a different interpretation. In that case, the first Rayleigh wave, at ~650 seconds (2.95 km/s) is much larger in the seismogram, and corresponds to the large clear peak of the correlation plotted vs. time. That arrival however has a measured backazimuth of 165°, 64° off azimuth to the south. Given the large azimuth deviation and high velocity, this could be a quasi-Love wave, that is a Love wave refracted toward more vertical polarization by a strong velocity discontinuity dipping perpendicular to the propagation, such as the basement of the Tarim Basin. Alternately, the polarization could just be due to complexity of the original Rayleigh wavefront due to the basin.

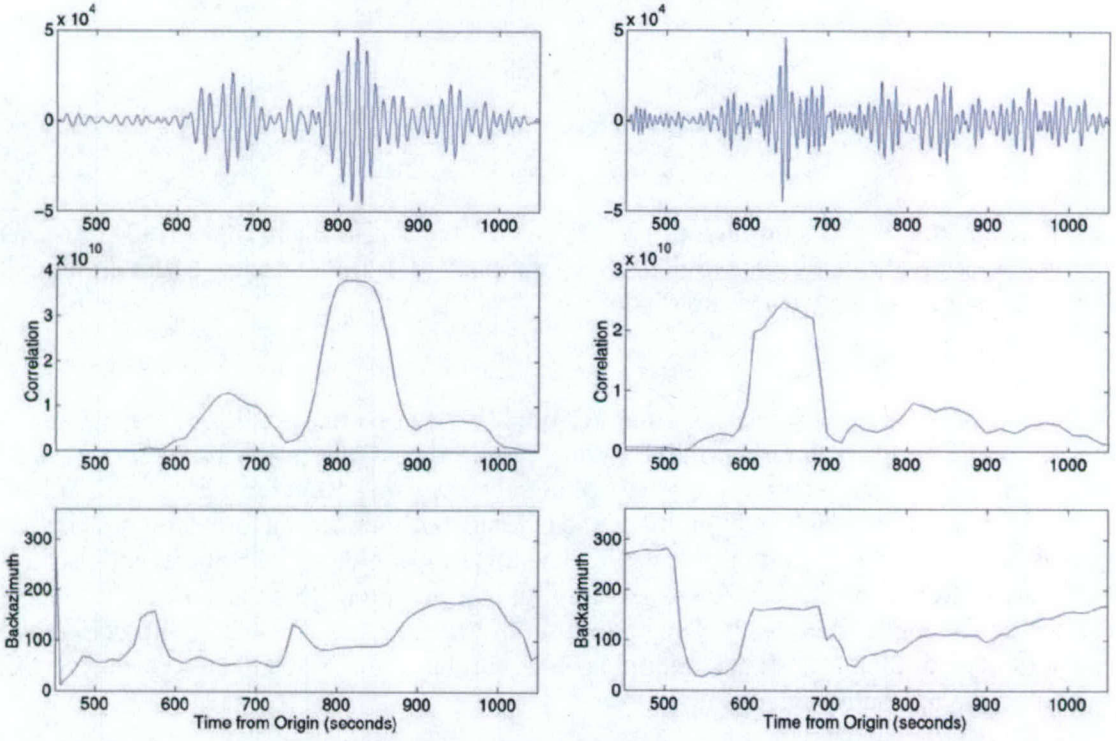

Figure 36. Vertical component surface waves (top row) for the problem path across the Tarim Basin. The second row shows the correlation of the Hilbert transformed radial with the vertical, which identifies Rayleigh waves. The third row shows the backazimuth vs time. The left column is for data filtered from 10 to 20 seconds period, and the right is for data filtered from 5 to 10 seconds period. The great circle back azimuth is 101 degrees.

A fan section of events recorded at the KNET station ULHL provides a look at variations in the characteristics of records with paths through different parts of the basin (Figures 37 and 38). Figure 37 shows the different paths through the basin. We focus on the events within the circle in the lower right.

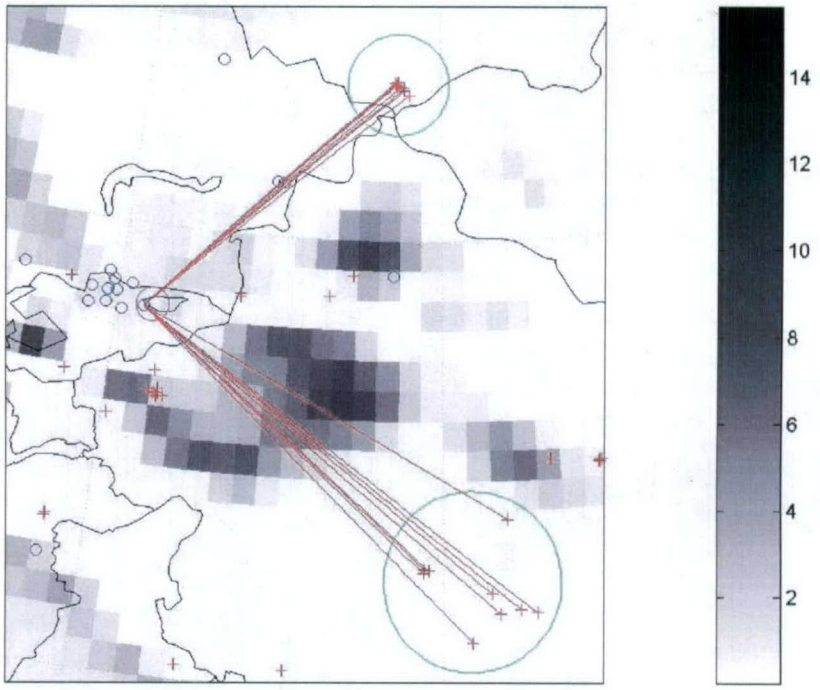

Figure 37. Location of paths through different parts of the Tarim Basin (red lines) from events (within green circle at lower right) to the KNET station ULHL (blue circle). Sediment thickness in kilometers is indicated by grayscale shading.

Figure 38 shows 3-component records, filtered from 20 to 30 seconds period, of the events with paths through the Tarim Basin, shown in Figure 37. Records are ordered by backazimuth, which is listed to the right of the records. Traces are plotted on the same scale for each event's records, normalized by the radial amplitude. In this passband, most of the records look similar. The two exceptions are the top and bottom set of traces. The uppermost record, from the event passing closest to the center of the basin, shows high amplitude signal preceding the surface waves, which may be from an earlier event. The bottom set of traces is for the event coming closest to the southern edge of the basin. It has multiple peaks, similar to the problem case of Figure 33, which skirted the northern edge of the basin.

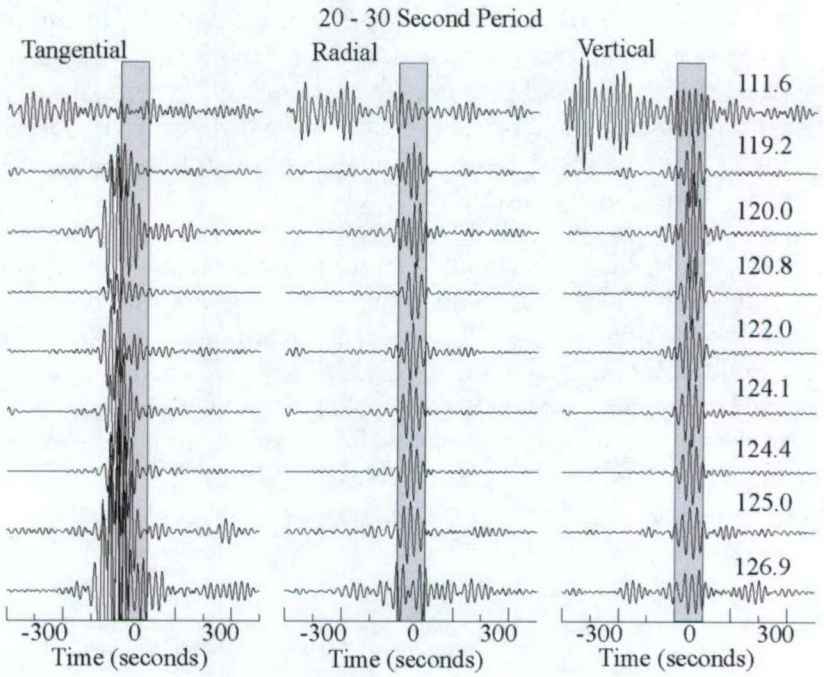

Figure 38. 3-component records, filtered from 20 to 30 second period, arranged by backazimuth of the events within the green circle in the lower right of Figure 37. Records are centered at 2.8 km/sec (0 seconds on the time axis). Fifty seconds either side of the center are highlighted in each record to facilitate comparison.

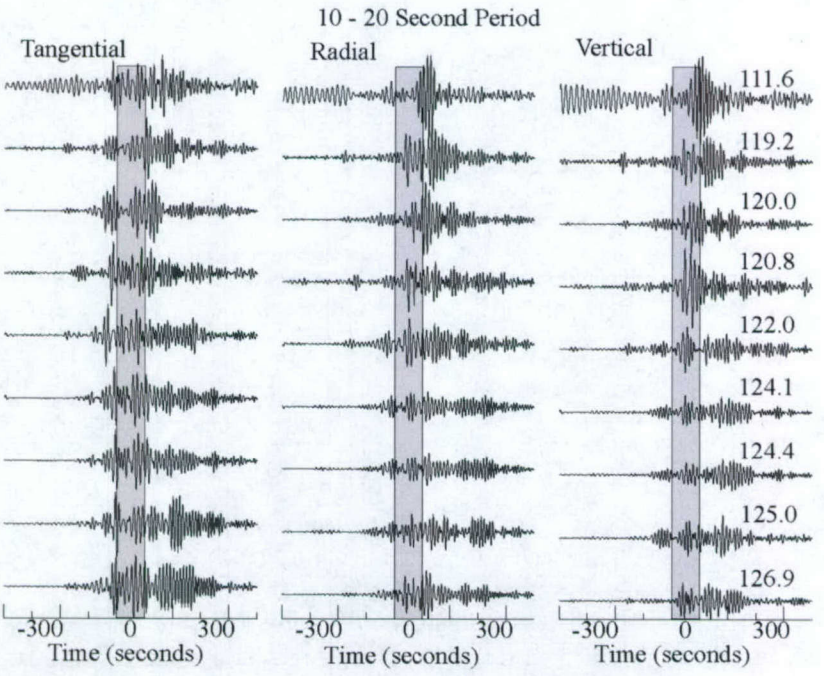

Figure 39. Same as Figure 38, except filtered from 10 to 20 second period.

Figure 39 shows the same records filtered from 10 to 20 second period. The influence of the basin appears to be stronger, as the records vary much more. In some, for example at 125° backazimuth, it appears that there could be quasi-Love waves on the vertical component. Many of the records appear to be complicated by multipathing. The differences between records however, are not simple, systematic, or easily predictable. In the following we use Rayleigh wave polarization to try to resolve the different arrivals.

Figure 40 (left column) shows the vertical and Hilbert transformed radial records, filtered from 20 to 30 seconds period, of Figures 37-39. The right column shows their crosscorrelation. This differs from the example in Figure 36, which showed the maximum crosscorrelation in each time window found at different backazimuths for each window. Since the crosscorrelation is formed using the radial component rotated to the great circle path, this example is biased toward identifying Rayleigh waves arriving at the predicted backazimuth. In this frequency band, there is little ambiguity about the phase selection and arrival time for most paths. However, in the 126.9° case (bottom row), there is an early, possible quasi-Love wave arrival and a later, possibly multi-pathed arrival in the vertical seismogram, but there is only one distinct arrival in the correlation.

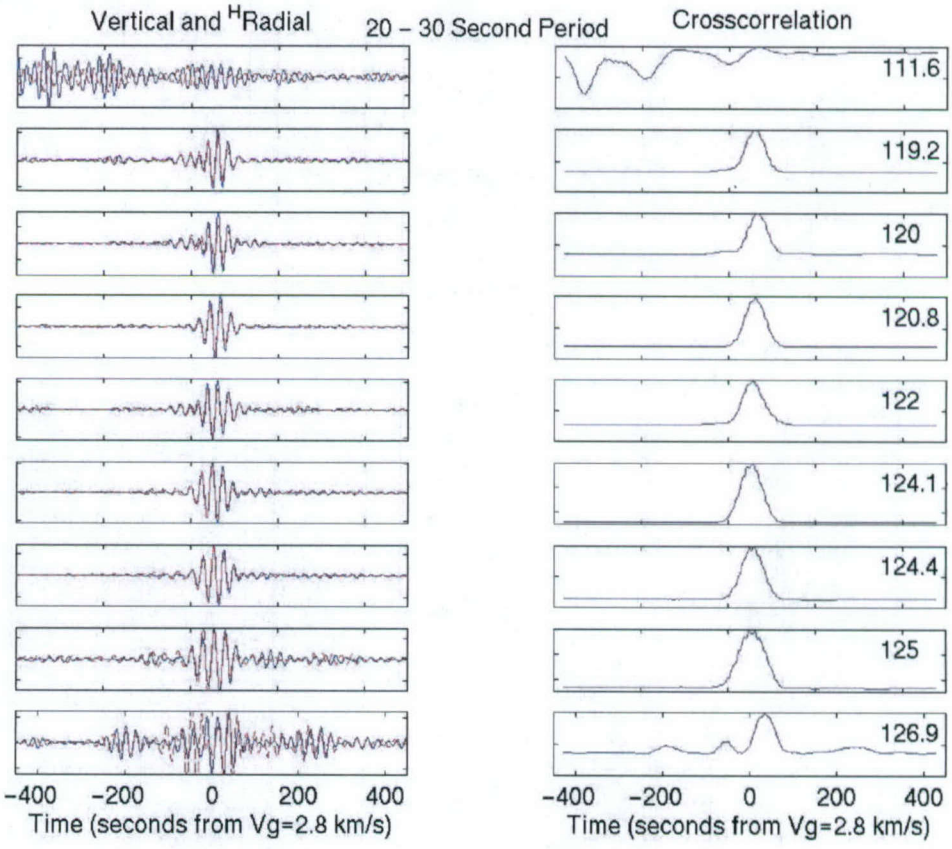

Figure 40. Vertical (blue) and Hilbert transformed radial (dotted red) seismograms (left) filtered from 20 to 30 seconds period, and their correlation over a series of tightly overlapping 75 second windows.

Figure 41 is similar to Figure 40, but for 10 to 20 seconds period. These records are more complex than those at 20 to 30 seconds period in Figure 6.11, and the correlations of the Hilbert transformed radial and the vertical seismograms are also more complex. Starting this time at the southern end, the vertical component record at 126.9° (bottom row), has 3 distinct arrivals, but the correlation shows only two are consistent with a Rayleigh wave arriving at or near the predicted backazimuth. The next 4 records to the north also have two distinct arrivals in the correlation vs. time. Those at 124.1° and 124.4° backazimuth have some additional complexity, but less than the seismograms. The seismograms also appear to have very early quasi-Love wave arrivals, which are diminished in the crosscorrelations. To distinguish between the two Rayleigh waves, and associated peaks from one record to the next, we need to do more. We could apply the algorithm used to make in Figure 36, to estimate the backazimuth associated with each Rayleigh wave coming in near the predicted backazimuth and directly estimate the dispersion curve from the correlations. Alternately, we could estimate the backazimuth of each arrival peak shown in Figure 35. We could then eliminate from consideration any arrivals not arriving from a direction near the predicted backazimuth, and use just the remaining peaks.

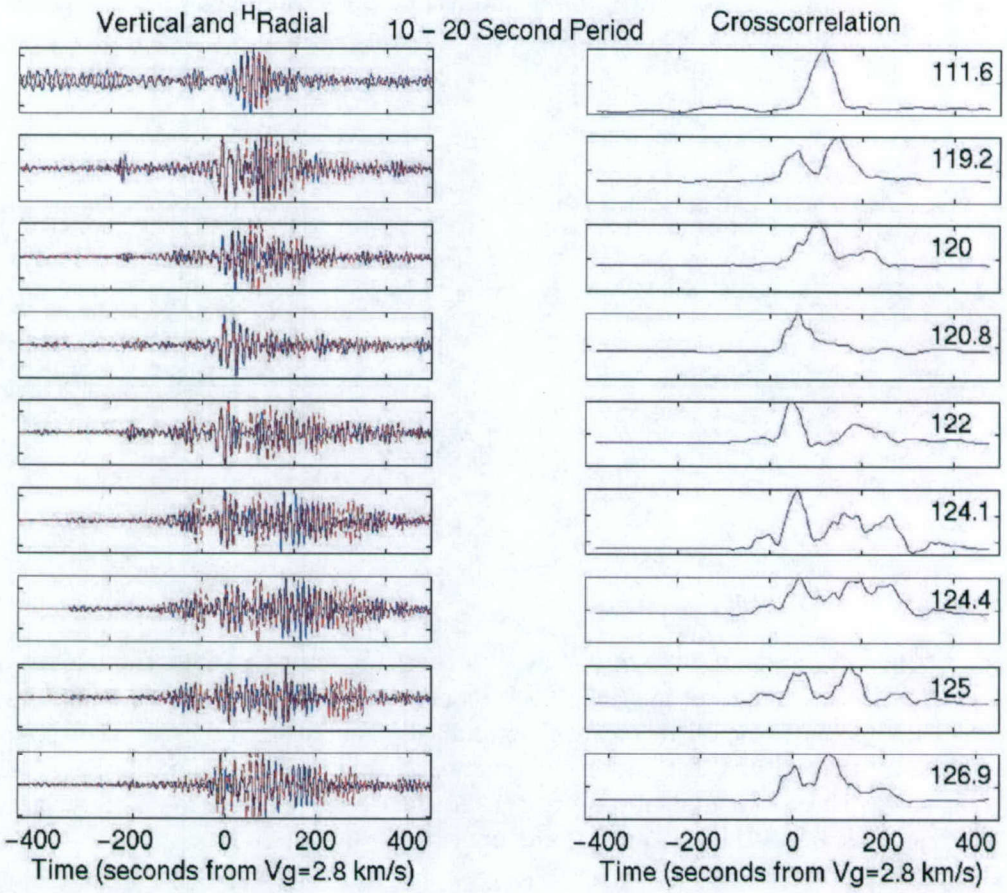

Figure 41. Vertical (blue) and Hilbert transformed radial (dotted red) seismograms (left) filtered from 10 to 20 seconds period, and their correlation over a series of tightly overlapping 45 second windows.

We can examine the utility of such approaches by determining the backazimuth that provides the maximum crosscorrelation of the vertical and Hilbert transformed radial vs. time, as in Figure 36, for the peaks of the two southernmost records of Figure 41, which are at 1,771 km (126.9° backazimuth event) and 1457 km (125.0° backazimuth event) respectively. Figure 42 shows those results. These crosscorrelation plots represent the crosscorrelation at the rotation of the horizontal components that maximizes the crosscorrelation. Those of Figure 41 are the crosscorrelation using just the radial component given the theoretical backazimuth. The first peak of the southernmost records' crosscorrelation vs. time from the origin arrives at 2.78 km/s (637 seconds) and is 47° off azimuth to the south. Thus it is either refracted strongly off the great circle path, or is a quasi-Love wave, or perhaps both such arrivals overlap. The second, at 2.48 km/s (715 seconds) is just 4° off azimuth to the south, and so represents the direct Rayleigh wave. The same analysis on the next event to the north, at 125° backazimuth, finds that the first peak of the crosscorrelation, at 2.66 km/s (548 seconds) is 45° off azimuth to the south. Thus it appears to correspond with the first arrival of the next event to the south. The second arrives at 2.26 km/s (645 seconds) and is 23° off azimuth to the south. This event's path is through a deeper part of the basin, so it has slower propagation and greater deflection (toward the shallower sediments further south). This demonstrates that polarization can be used to identify and associate distinct arrivals between events, and should improve the determination of accurate and appropriate group velocity curves.

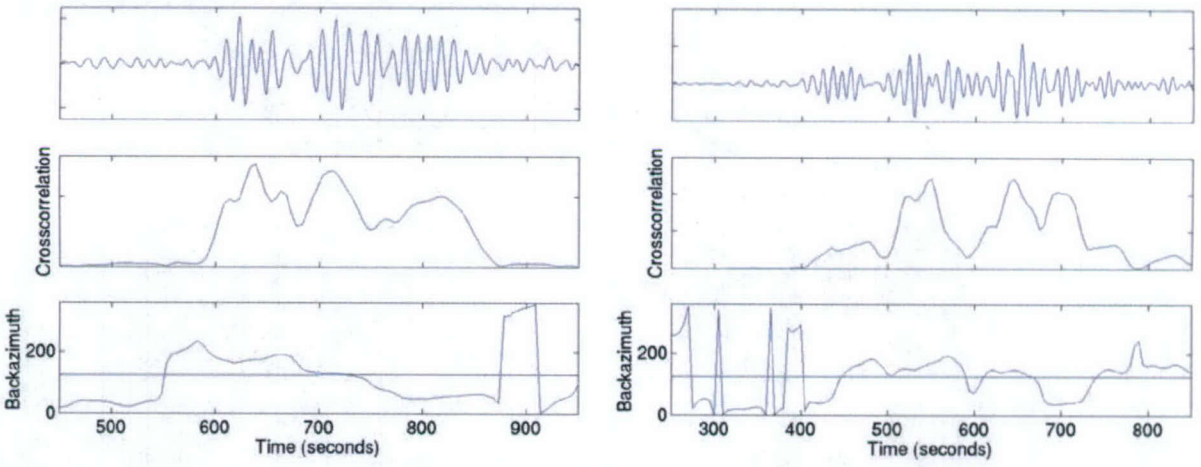

Figure 42. Vertical component surface waves (top row) for the two southernmost records of Figure 41 (126.9° backazimuth on the left, 125.0° backazimuth on the right), the correlation of the horizontal component rotated to the backazimuth that maximizes the crosscorrelation with the Hilbert transformed vertical for successive windows (middle row), and that backazimuth vs time (bottom row). The horizontal line indicates the theoretical backazimuth. Data are filtered from 10 to 20 seconds period. Time is seconds from origin.

7 CONCLUSIONS AND RECOMMENDATIONS

The dispersion models developed in this study can be used to find the phase and group velocities between any two points on the earth at any frequency. These models are available to all researchers on request, and have been provided for use in a number of other research projects. The dispersion models depend on dispersion data for accuracy, and so can be improved as more dispersion data becomes available. We therefore recommend continuation of this iterative process. As more data becomes available, particularly from regions or in frequency bands currently sparsely covered, we can improve the models and in turn provide these predictions for comparison with and as a starting point for new surface wave studies in regions of interest.

The azimuth estimation algorithm currently used at the International Data Center should be replaced with the Selby/Chael algorithm that was implemented and tested in this project. The procedure can be used together with the dispersion test to reduce the detection threshold for automatic surface wave processing by relaxing the requirements of the dispersion test when the azimuth estimate is consistent with an event hypothesis with a high correlation value.

The path corrected spectral magnitude provides a "regional M_s" which has been a long-term goal of this program. The path corrected spectral magnitude can be measured over any frequency band, however for discrimination purposes, surface waves should be measured at periods greater than 10 seconds. Periods of 10 seconds and longer can be measured even at very close range, and there is only a small S/N improvement, if any, at shorter periods. Measurement at higher frequencies risks error in discrimination due to the decrease in earthquake spectral amplitude relative to explosions at higher frequencies, particularly for events for which shallow depth is uncertain. A path corrected time domain magnitude can be derived by combining the path corrected spectral magnitude with the Russell (2004) surface wave magnitude $M_{s(b)}$.

Additional work is needed regarding how to model and invert surface wave amplitude and dispersion in regions of complex earth structure. In particular, surface waves traveling at near grazing incidence to strong heterogeneities may exhibit amplitude variations not only due to focusing/defocusing, but also due to interference of arrivals taking multiple paths through the medium. Similarly, dispersion measurements are complicated by the presence of distinct, multiple arrivals at short periods and interfering arrivals that cannot be separated at longer periods. Some of this behavior can be modeled by incorporating scattering theory into the inversion procedure (e.g. Zhou et al., 2004), however the interference is so strong in some cases that it may not be possible to model it accurately with approximate methods. A partial solution is to use waveform polarization to identify waves traveling closest to a great circle path and to use only frequency bands where polarization is reasonably consistent with a great circle path and interference between multiple arrivals is not present or can be removed.

8 DATA DELIVERABLE

Two data deliverables are provided together with this final report. They are:

1. The final set of earth models, dispersion curves and other derived data. These are contained in compressed tar file "LP_2005_Mar.tar.Z". Information on data format is included in the delivery.

2. The maxpmf program compiled for Sun Solaris, and the maxpmf man page. These are contained in compressed tar file "maxpmf_5.3.tar.Z".

These data deliverables may be obtained from the contracting office or from the authors.

9 REFERENCES

Baker, G. Eli and Jeffry L. Stevens (2004), "Backazimuth estimation reliability using surface wave polarization," Geophysical Research Letters, v. 31, L09611, doi:10.1029/2004GL019510.

Bassin, C., G. Laske, and G. Masters (2000), The Current Limits of Resolution for Surface Wave Tomography in North America, *EOS Trans AGU* 81, F897.

Bonner, J. L., D. T. Reiter, D. G. Harkrider, and S. Russell (2004), "Development of a time-domain, variable-period surface wave magnitude measurement procedure for application at regional distances," in *Proceedings of the 26th Annual Seismic Research Review, Orlando, FL, 21-23 September 2004.*

Chael, E. (1997), An automated Rayleigh-Wave Detection Algorithm, *B.S.S.A.*, **87**, 157-163.

Dziewonski, A. M., J. Bloch, and M. Landisman (1969), "A new technique for the analysis of transient seismic signals", *Bull. Seism. Soc. Am.*, v. 59, pp. 427-444.

Ekstrom, G., A. M. Dziewonski, G. P. Smith, and W. Su (1996), Elastic and Inelastic Structure Beneath Eurasia, in *Proceedings of the 18th Annual Seismic Research Symposium on Monitoring a Comprehensive Test Ban Treaty, 4-6 September, 1996*, Phillips Laboratory Report PL-TR-96-2153, July, ADA313692, 309-318.

Engdahl, E. R., R. van der Hilst, and R. Buland (1998), Global Teleseismic Earthquake Relocation with Improved Travel Time and Procedures for Depth Determination, *Bull. Seismol. Soc. Am.* 88, 722 - 743.

Fisher, N.I. (1993), Statistical Analysis of Circular Data, Cambridge Univ. Press.

Harkrider, D. G., J. L. Stevens, and C. B. Archambeau (1994), "Theoretical Rayleigh and Love waves from an Explosion in Prestressed Source Regions," *Bull. Seism. Soc. Am.*, v. 84, pp. 1410-1442.

Huang, Z., W. Su, Y. Peng, Y. Zheng, and H. Li (2003), Rayleigh Wave Tomography of China and Adjacent Regions. *J. Geophys. Res.* 108(B3), 2073, doi: 10.1029/2001JB001696.

Kennett, B. L. N. E. R. Engdahl, and R. Buland (1995), Constraints on Seismic Velocities in the Earth from Travel Times, *Geophys. J. Int.* 122, 108-124.

Laske, G. and G. Masters (1997), A Global Digital Map of Sediment Thickness, *EOS Trans. AGU* 78, F483.

Laske, G., G. Masters, and C. Reif, Crust 2.0 (2001): A New Global Crustal Model at 2x2 Degrees, http://mahi.ucsd.edu/Gabi/rem.html.

Levin, V. and J. Park (1998), Quasi-Love phases between Tonga and Hawaii: Observations, simulations and explanations, *JGR*, **103**, pp 24321-24331.

Levshin, Anatoli L., Jeffry L. Stevens, Michael H. Ritzwoller, David A. Adams, and G. Eli Baker (2003), "Improvement of Detection and Discrimination Using Short Period (7s-15s) Surface Waves in W. China, N. India, Pakistan and Environs," Final report submitted to Defense Threat Reduction Agency, SAIC Report No. 03/2008, CU Project No. 1532378, April.

Levshin, A. L., M. H. Ritzwoller, and S. S. Smith (1996), "Group Velocity Variations Across Eurasia," in *Proceedings of the 18th Annual Seismic Research Symposium on Monitoring A Comprehensive Test Ban Treaty,* Phillips Laboratory Report PL-TR-96-2153.

Mancilla, Flor de Lis, "Surface wave dispersion about the New Madrid Region," M. Sci. Thesis, Saint Louis University, 2001.

Marshall, P. D. and P. W. Basham (1972), Discrimination Between Earthquakes and Underground Nuclear Explosions Employing an Improved M_s Scale, *Geophys. J. R. astr. Soc.* 28, 431-458.

McGarr, A. (1969), "Amplitude Variations of Rayleigh Waves – Propagation Across A Continental Margin," *Bull. Seism. Soc. Am.*, v. 59, pp. 1281-1305.

Mitchell, B. J., L. Cong and J. Xie, (1996), "Seismic Attenuation Studies in the Middle East and Southern Asia", St. Louis University Scientific Report No. 1, PL-TR-96-2154, ADA317387.

Mooney, W., G. Laske, and G. Masters (1998), Crust 5.1: A Global Crustal Model at 5x5 Degrees, *J. Geophys. Res.* 103, 727-747.

Rezapour, M. and R. G. Pearce (1998), "Bias in Surface-Wave Magnitude Ms due to Inadequate Distance Corrections," *Bull. Seism. Soc. Am.*, v. 88, pp. 43-61.

Ritzwoller, M. H., A. L. Levshin, L. I. Ratnikova, and D. M. Tremblay (1996), "High Resolution Group Velocity Variations Across Central Asia," in Proceedings of the 18th Annual Seismic Research Symposium On Monitoring A Comprehensive Test Ban Treaty.

Ritzwoller, M. H., N. M. Shapiro, M. P. Barmin, and A. L. Levshin (2002), "Global surface wave diffraction tomography", *J. Geophys. Res.*, **107**, 2335, doi:10.1029/2002JB001777.

Ritzwoller, M.H., O.Y Vdovin, and A.L. Levshin (1999), "Surface wave dispersion across Antarctica: A first look", Antarctic J. U.S., in press.

Russell, D. R. (2004), "Theoretical analysis of narrow-band surface wave magnitudes," AFTAC technical report AFTAC-TR-04-004, June.

Selby, N.D. (2001), Association of Rayleigh waves using backazimuth measurements: application to test ban verification. *Bull. Seism. Soc. Am.*, **91**, 580-593.

Smart, E. (1978), A three-component, single-station, maximum-likelihood surface wave processor, *Geotech Report No.* SDAC-TR-77-14.

Smart, E. and H. Sproules (1981), Regional phase processors, *Geotech Report No.* VSC-TR-81-19.

Stevens, J. L. (1986), "Estimation of Scalar Moments From Explosion-Generated Surface Waves," *Bull. Seism. Soc. Am.*, v. 76, pp. 123-151.

Stevens, J. L. and S. M. Day (1985), "The Physical Basis of the mb:Ms and Variable Frequency Magnitude Methods for Earthquake/Explosion Discrimination," *Journal of Geophysical Research*, v. 90, pp. 3009-3020.

Stevens, J. L. and D.A. Adams (2000), Improved Surface Wave Detection and Measurement Using Phase-Matched Filtering and Improved Regionalized Models, in *Proceedings of the 22nd Annual DOD/DOE Seismic Research Symposium, 12-15 September 2000*, 145-154.

Stevens, J.L., D. Adams, and G.E. Baker (2001), Improved surface wave detection and measurement using phase-matched filtering with a global one-degree dispersion model, *Proceedings of the 23rd Seismic Research Review: Worldwide Monitoring of Nuclear Explosions*, 420-430.

Stevens, J. L., D. A. Adams, and E. Baker (2002), Improved Surface Wave Dispersion Models and Azimuth Estimation Techniques, in *Proceedings of the 24th Annual DOD/DOE Seismic Research Symposium, 17-19 September 2002*, 552-561.

Stevens, J. L., D. A. Adams, and M. G. Eneva (2003), "Improved Surface Wave Dispersion Models and Amplitude Measurements," *Proceedings of the 25th Annual Seismic Research Review*, Tucson, AZ, 23-25 September, 2003.

Stevens, J. L., D. A. Adams, G. E. Baker, M. G. Eneva and H. Xu (2004), "Improved Surface Wave Dispersion Models, Amplitude Measurements and Azimuth Estimates," *Proceedings of the 26th Annual Seismic Research Review*, Orlando, FL, 21-23 September 2004.

Stevens, J. L. and K. L. McLaughlin (1996), "Regionalized Maximum Likelihood Surface Wave Analysis," Maxwell Technologies Technical Report PL-TR-96-2273, SSS-DTR-96-15562, September.

Stevens, J. L., and K. L. McLaughlin (1988), "Analysis of surface waves from the Novaya Zemlya, Mururoa, and Amchitka test sites, and maximum likelihood estimation of scalar moments from earthquakes and explosions," S-CUBED technical report SSS-TR-89-9953, September.

Stevens, J. L. and K. L. McLaughlin (2001), Optimization of Surface Wave Identification and Measurement, *Pure Appl. Geophs.* 158, 1547-1582.

Stevens, J. L. and J. R. Murphy (2001), "Yield Estimation from surface wave amplitudes," *Pure and Applied Geophysics*, **158**, 2227-2251.

Vdovin, O. Y., J. A. Rial, M. H. Ritzwoller, and A. L. Levshin (1999), "Group-velocity tomography of South America and the surrounding oceans", *Geophys. J. Int.*, 136, 324-330.

Yang, X., S. R. Taylor, H. J. Patton, M. Maceira, and A. A. Velasco (2002), Evaluation of Intermediate-Period (10- to 30-sec) Rayleigh-Wave Group Velocity Maps for Central Asia, in *Proceedings of the 24th Annual DOD/DOE Seismic Research Symposium, 17-19 September 2002,* 609-617.

Zhou, Y., F. A. Dahlen and G. Nolet (2004), "Three-dimensional sensitivity kernels for surface wave observables," *Geophys. J. Int.*, **158**, 142-168.